AD__________________

Award Number: DAMD17-00-1-0217

TITLE: Breast Cancer Diagnosis Using Ultrasound and Diffusive Light

PRINCIPAL INVESTIGATOR: Quing Zhu, M.D.

CONTRACTING ORGANIZATION: University of Connecticut
Storrs, Connecticut 06269-1113

REPORT DATE: September 2001

Reproduced From
Best Available Copy

TYPE OF REPORT: Annual

PREPARED FOR: U.S. Army Medical Research and Materiel Command
Fort Detrick, Maryland 21702-5012

DISTRIBUTION STATEMENT: Approved for Public Release;
Distribution Unlimited

The views, opinions and/or findings contained in this report are those of the author(s) and should not be construed as an official Department of the Army position, policy or decision unless so designated by other documentation.

20020118 194

REPORT DOCUMENTATION PAGE

Form Approved
OMB No. 074-0188

Public reporting burden for this collection of information is estimated to average 1 hour per response, including the time for reviewing instructions, searching existing data sources, gathering and maintaining the data needed, and completing and reviewing this collection of information. Send comments regarding this burden estimate or any other aspect of this collection of information, including suggestions for reducing this burden to Washington Headquarters Services, Directorate for Information Operations and Reports, 1215 Jefferson Davis Highway, Suite 1204, Arlington, VA 22202-4302, and to the Office of Management and Budget, Paperwork Reduction Project (0704-0188), Washington, DC 20503

1. AGENCY USE ONLY (Leave blank)	**2. REPORT DATE** September 2001	**3. REPORT TYPE AND DATES COVERED** Annual (15 Aug 00 - 14 Aug 01)

4. TITLE AND SUBTITLE
Breast Cancer Diagnosis Using Ultrasound and Diffusive Light

5. FUNDING NUMBERS
DAMD17-00-1-0217

6. AUTHOR(S)
Quing Zhu, M.D.

7. PERFORMING ORGANIZATION NAME(S) AND ADDRESS(ES)
University of Connecticut
Storrs, Connecticut 06269-1113

E-Mail: zhu@engr.uconn.edu

8. PERFORMING ORGANIZATION REPORT NUMBER

9. SPONSORING / MONITORING AGENCY NAME(S) AND ADDRESS(ES)

U.S. Army Medical Research and Materiel Command
Fort Detrick, Maryland 21702-5012

10. SPONSORING / MONITORING AGENCY REPORT NUMBER

11. SUPPLEMENTARY NOTES
Report contains color

12a. DISTRIBUTION / AVAILABILITY STATEMENT
Approved for Public Release; Distribution Unlimited

12b. DISTRIBUTION CODE

13. ABSTRACT ***(Maximum 200 Words)***

The main goal of this study is to evaluate a novel imaging system and method that combines ultrasound with near infrared diffusive light to increase the sensitivity and specificity of breast cancer detection. The specific tasks of this study are 1) to refine our existing NIR optical imaging system hardware toward high signal-to-noise ratio and fast data acquisition; 2) to implement imaging software for clinical studies; 3) to optimize the combined probe design through simulation and phantom experiments; and 4) to validate the combined imaging in cancer detection and diagnosis through clinical studies.

We have successfully completed the tasks 1 to 3 during the first year of this study and have started task 4. As a result of this study, two journal papers and 8 proceeding papers have been published or accepted.

14. SUBJECT TERMS
Breast Cancer

15. NUMBER OF PAGES
69

16. PRICE CODE

17. SECURITY CLASSIFICATION OF REPORT Unclassified	**18. SECURITY CLASSIFICATION OF THIS PAGE** Unclassified	**19. SECURITY CLASSIFICATION OF ABSTRACT** Unclassified	**20. LIMITATION OF ABSTRACT** Unlimited

NSN 7540-01-280-5500

Standard Form 298 (Rev. 2-89)
Prescribed by ANSI Std. Z39-18
298-102

Table of Contents

SF 298..

Table of Contents..1

Introduction...2

Body..3

Key Research Accomplishments..6

Conclusions...7

References..8

Appendices and list of presentations...9

Introduction:

Recently optical diagnostics based on diffuse near-infrared (NIR) light has been employed in breast cancer detection [1-4]. Optical spectroscopy and imaging of body structure and function is made possible by a spectral window that exists within tissues in the 700 - 900 nm region (near-infrared (NIR)), in which photon transport is dominated by scattering rather than absorption. Thus, to a very good approximation, NIR photons diffuse through relatively thick tissues. Compared with other imaging methods, the optical method has numerous advantages. NIR light has high specificity because certain characteristics differ in tumors and normal breast tissues: 1) The amount of blood needed to serve the tumor's metabolic needs is increased over that of normal background tissue; 2) Hemoglobin desaturation in tumors is increased due to the high oxygen demand of cancers [5]; 3) Light scattering of the tumor is enhanced due to the increased mitochondria population with respect to the background of normal cells [6]; 4) The angiogenesis phenomenon [7] allows tumor identification by observing the delivery of contrast agents, such as the well-characterized NIR absorber indocyanine green (ICG), through the permeable vascular beds to the extravascular space surrounding the tumor. In addition, the NIR device requires relatively low manufacturing and operating costs, NIR light is non-invasive to the human body, and the device is compact and easily portable. As a potential diagnostic, however, diffused NIR light imaging and spectroscopy suffer from low spatial resolution due to the diffusive nature of photon density waves. Current instruments can distinguish simple structures of approximately 1 cm in size, but sharp edges are typically blurred by a few millimeters [2]. In addition, imaging reconstruction is based on inverse scattering approaches [8-10] and the inverse problem is in general underdetermined and ill-posed. Thus while the optical method offers new routes to tumor specificity, the relatively low resolution and difficulties in image reconstruction make it difficult to take full advantage of this contrast.

The concept of pulse-echo ultrasound imaging is well known. Ultrasound has many advantages: its manufacturing and operating costs are low; it is non-invasive to the human body and it provides high-resolution real-time images. Current state-of-the-art breast scanners can detect small lesions of several millimeters in size [13]. Ultrasound is frequently used in conjunction with mammography to differentiate simple cysts from solid lesions. When the criteria for a simple cyst are strictly adhered to, the accuracy of ultrasound is 96%-100%. However, the ultrasound appearance of benign and malignant lesions has considerable overlapping features [11-12], which has prompted many radiologists to recommend biopsies on most solid nodules. This results in a large number of biopsies yielding normal or benign breast tissues.

We have developed a novel hybrid imaging technique, which combines the high contrasts of NIR imaging in distinguishing between normal, benign and malignant tissues with the high spatial resolution inherent in ultrasound imaging. This hybrid imaging method provides a new way to utilize optical contrast and ultrasound imaging capability [14-17].

In this DOD ARMY sponsored study, we proposed to achieve the flowing objectives

1) to refine our existing NIR optical imaging system hardware toward high signal-to-noise ratio and fast data acquisition (task 1);
2) to implement to imaging software for clinical studies (task 1)
3) to optimize the combined probe design through simulation and phantom experiments (task 1);
4) to validate the combined imaging in cancer detection and diagnosis through clinical studies (task 2).

We have successfully completed task 1 proposed in the application and has started the task 2 by recruiting breast cancer patients. We expect to start clinical studies in a month.

Body

Under the supports of DOD ARMY we have completed the combined probe by co-axially deploying optical and ultrasound probes simultaneously. This combined probe can partially overcome the lesion mapping uncertainty problem encountered in our preliminary clinical studies where optical and ultrasound probes were used separately to scan deformable breasts [14]. The optical probe consists of 12 dual wavelength sources and 8 optical detectors [17], and the sources and detectors are coupled through optical fibers to a hand-held probe shown in Figure 1(a). A commercial ultrasound probe (7 MHz linear array) is simultaneously deployed in the middle of the combined probe. With this combined probe, we can demonstrate the advantage of dual-modality diagnosis. The picture of our NIR scanner is shown in Figure 1(b). All the imaging algorithms are implemented in the software and the system will be used to perform pilot clinical studies.

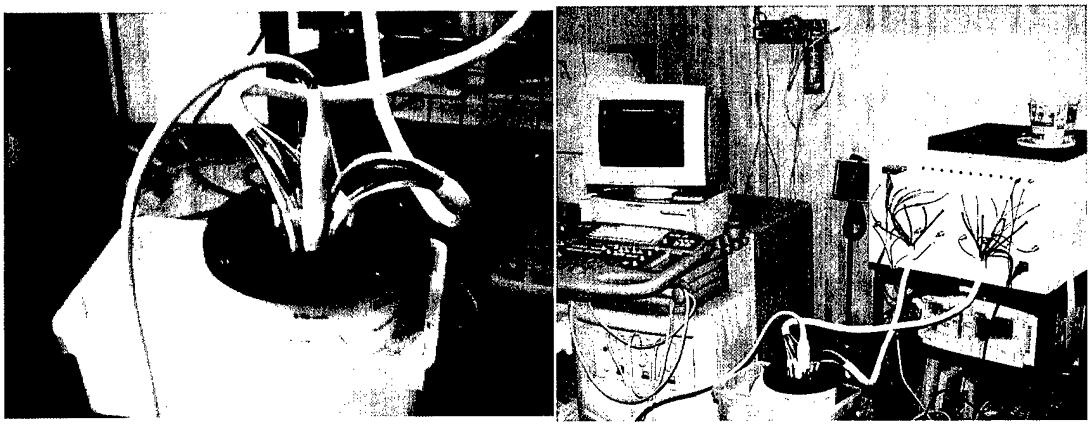

Figure 1. (a). Our combined probe with NIR sensors deployed at the periphery and a 1-D commercial ultrasound array located in the middle. (b). Commercial ultrasound scanner (left), our NIR system (right) and the combined probe (middle).

In addition to complete the above proposed tasks, we have also done three dimensional simultaneous ultrasound and NIR imaging and co-registration in phantom tests. In the on-going clinical studies, conventional ultrasound images are obtained in x-z planes and NIR images are in x-y planes. Therefore, the ultrasound and NIR imaging planes are orthogonal to each other. Early detection of breast cancers requires simultaneous ultrasound and NIR imaging at the same imaging plane, **referred to as co-registration in the proposal**. Co-registration enables the use of lesion morphology provided by high-resolution ultrasound to improve the lesion optical property estimate. This task can be accomplished by simultaneously deploying a 2-D ultrasound array, which is capable of providing 3-D high-resolution volumetric images, and the multiple source and detector NIR array. We have built a simple 2-D ultrasound array consisting of 64 transducers, which were deployed simultaneously with the NIR source and detector fibers on the same probe, to demonstrate the feasibility of co-registration [17].

In Refs [16-17], we have demonstrated that with the *a priori* knowledge of lesion location and shape information provided by co-registered ultrasound, NIR imaging reconstruction can be localized within specified spatial and temporal regions. As a result, the reconstruction is over-determined because the total number of unknown optical properties is reduced significantly. In addition, the reconstruction is less sensitive to noise because the convergence can be achieved within a small number of iterations. We have conducted a series of experiments to assess the improvement on reconstructed optical absorption coefficients with the *a priori* target depth [16] and spatial location information [17]. For the experiments reported in Ref [16], we have shown that with the *a priori* target depth information provided by co-registered ultrasound, the accuracy of the reconstructed absorption coefficient has been improved by 15% and 30% on average, and the resolution measured at Full Width at Half Maximum has been improved by 24% and 41% on average for high and low contrast cases, respectively. The speed of reconstruction has been improved by 10 times on average. For the experiments reported in Ref [17], we have demonstrated that, with the guidance of *a priori* target temporal and spatial distributions, the iterative inversion algorithm converges very fast and only one iteration is needed to obtain accurate optical absorption coefficient. This result is very encouraging because there is no known robust stopping criterion in the literature to terminate iterative inversion algorithms. With the *a priori* knowledge from co-registered ultrasound, no further iterations are needed.

Our preliminary results of using co-registered ultrasound to improve the accuracy of estimated lesion optical properties are very encouraging. However, the image quality of our simple 2-D ultrasound array is far from commercial standard. We have upgraded our simple 2-D ultrasound array to commercial standards by incorporating a state-of-the-art 1.75D ultrasound array purchased from Tetrad Inc (see Fig.2a) and constructing the electronic data acquisition system (Fig.2b). The array consists of 1280 transducer elements and the ultrasound beam can be scanned in both x and y spatial directions. Preliminary results obtained from our high-resolution hybrid imaging system are given in Figure 3. Figure 3(a) is the ultrasound x-z image of a small emulated lesion (6 mm in diameter) of low optical contrast (absorption coefficient μ_a = 0.1 cm^{-1}) located 2.5 cm deep into the optical scattering medium ($\mu_s' = 6cm^{-1}$). Figure 3(b) is the ultrasound C-scan or spatial image of the target co-registered with NIR images shown in Fig.3 (c) and (d). Without ultrasound image guidance shown in (b), the μ_a image shown in Fig. 3(c) does not converge and two targets appear at wrong locations. With the ultrasound guidance shown in (b), the target shown in Fig.3 (d) appears at the correct location and the estimated μ_a is 86% of the true value. These preliminary results are very encouraging and suggest that the hybrid imaging method has a great potential to improve early detection by combining high spatial resolution of ultrasound and high contrast of optical imaging.

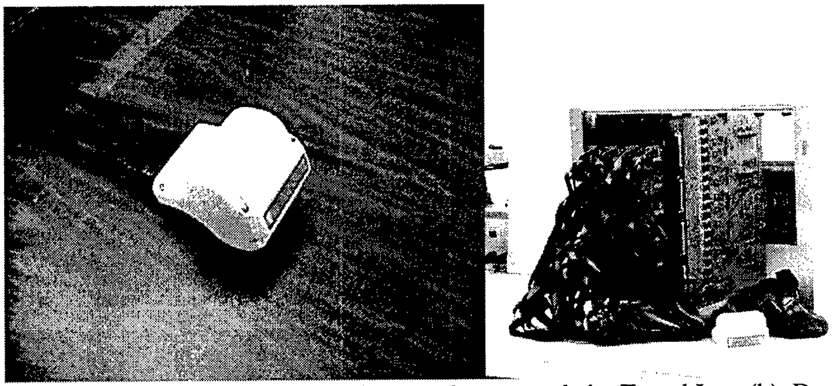

Figure 2. (a) The state-of-the-art 1.75-D ultrasound array made by Tetrad Inc. (b) Data acquisition system build by our group.

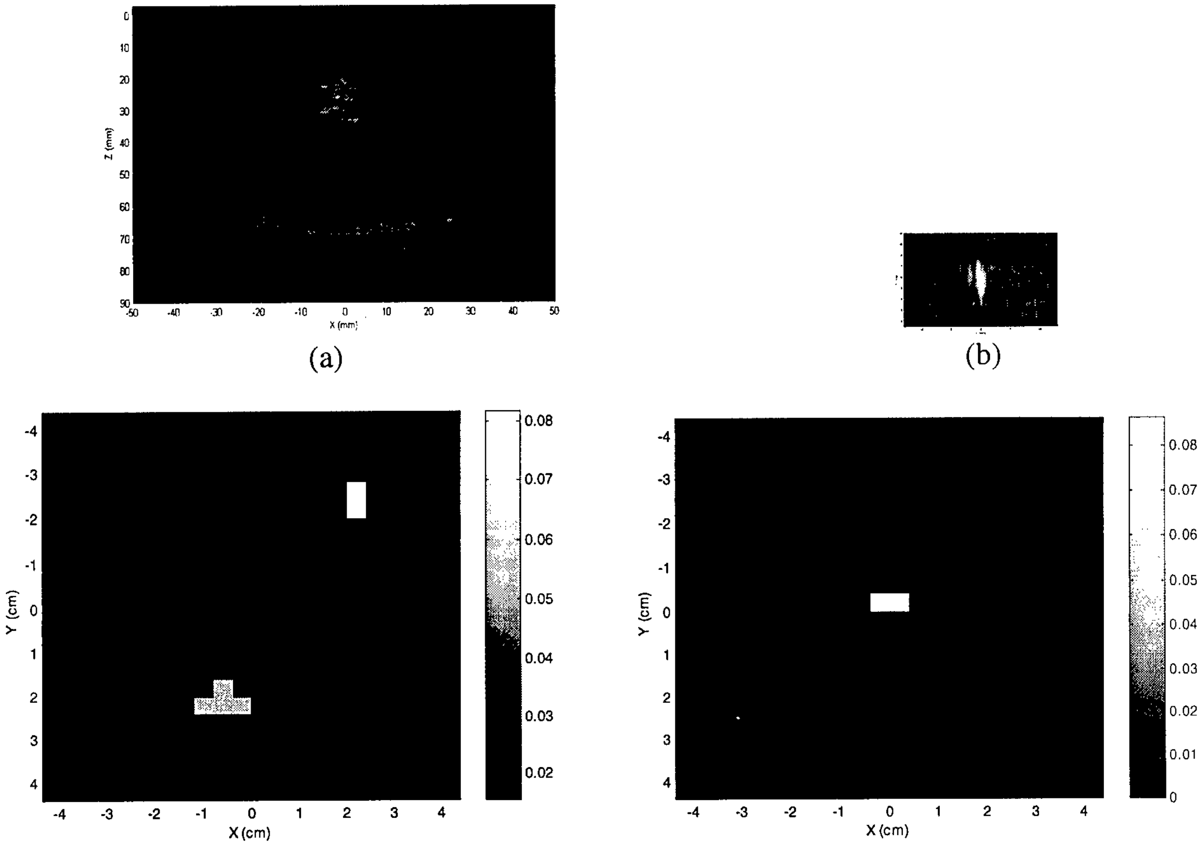

(a) (b)

(c) (d)

Figure 3. Ultrasound and optical images of a small (6mm in diameter) emulated tumor of low optical contrast (μ_a =0.1cm^{-1}) imbedded in the optical scattering medium (reduced scattering coefficient is μ_s' = 6 cm^{-1}). (a) Ultrasound image obtained in x-z scan, where x is the lateral direction and z is the propagation direction). The target is slightly echogenic and clearly seen. (b) C-scan or spatial x-y image of the ultrasound co-registered with NIR images shown in (c) and (d). The horizontal size of the image is 3 cm and the vertical size is 1.7 cm. The size is scaled to the same as in (c) and (d). (c) Reconstructed optical absorption image μ_a without ultrasound guidance. The small target should appear at the center location of the image, however, two targets appear at wrong locations. (d) With the guidance of co-registered ultrasound shown in (b), the reconstructed target appears at correct location and the reconstructed value is $\hat{\mu}_a$ =0.086 cm^{-1} which is 86% of the true value.

We have evaluated our new imaging method with an excised tumor using the system shown in Fig.1b. The tumor (9L model) was grown in a male Fisher rat and was excised immediately after the rat died from the anesthesia. The weight of the tumor was 3.6 grams and the volume was about 3.6 ml. The tumor was imbedded in the intralipid solution of 0.7% concentration, and the fitted background μ_a and μ_s' values were 0.021 cm^{-1} and 6.83 cm^{-1}, respectively. An ultrasound B-scan image of the tumor is shown in Figure 4, and the depth of the tumor evaluated at the center of the mass is about 2.5 cm. The tumor is acoustically heterogeneous which can be seen by the inhomogeneous echo pattern in the image. The absorption map of the tumor at 780 nm is shown in Figure 5, and the reconstructed absorption coefficient is 0.17 cm^{-1}. To evaluate the reconstructed absorption coefficients at different target volumes, we cut the tumor by half step by step and imaged the remaining portions of the tumor. The weights were 2.36, 1.75, 1.12, 0.59 grams, respectively. The reconstructed absorption coefficients were 0.18, 0.26, 0.27, 0.23 cm^{-1}, respectively. The changes in μ_a are primarily related to the heterogeneous structure of the tumor.

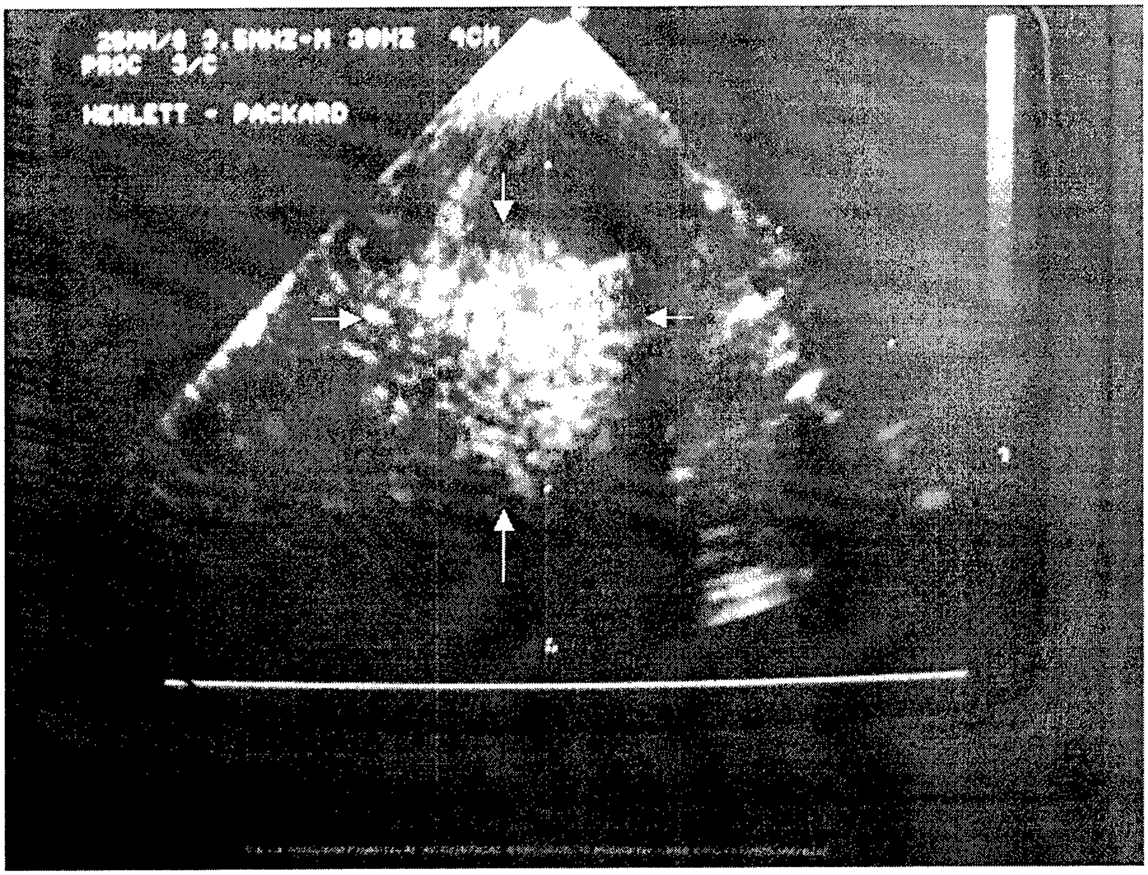

Figure 4 . Ultrasound B-scan of the excised tumor pointed by arrows. Tumor was imbedded in the intralipid of approximately 0.7% concentration and the fitted background μ_a and μ_s' values are 0.021 cm^{-1} and 6.83 cm^{-1}, respectively.

Key Research Accomplishments:

- refined our optical imaging system and implemented imaging software.
- optimized our combined probe by studying the optical and ultrasound sensor distributions.
- The combined method has been evaluated with phantoms and excised tumors and the improvement of the method compared with optical or ultrasound alone is significant.

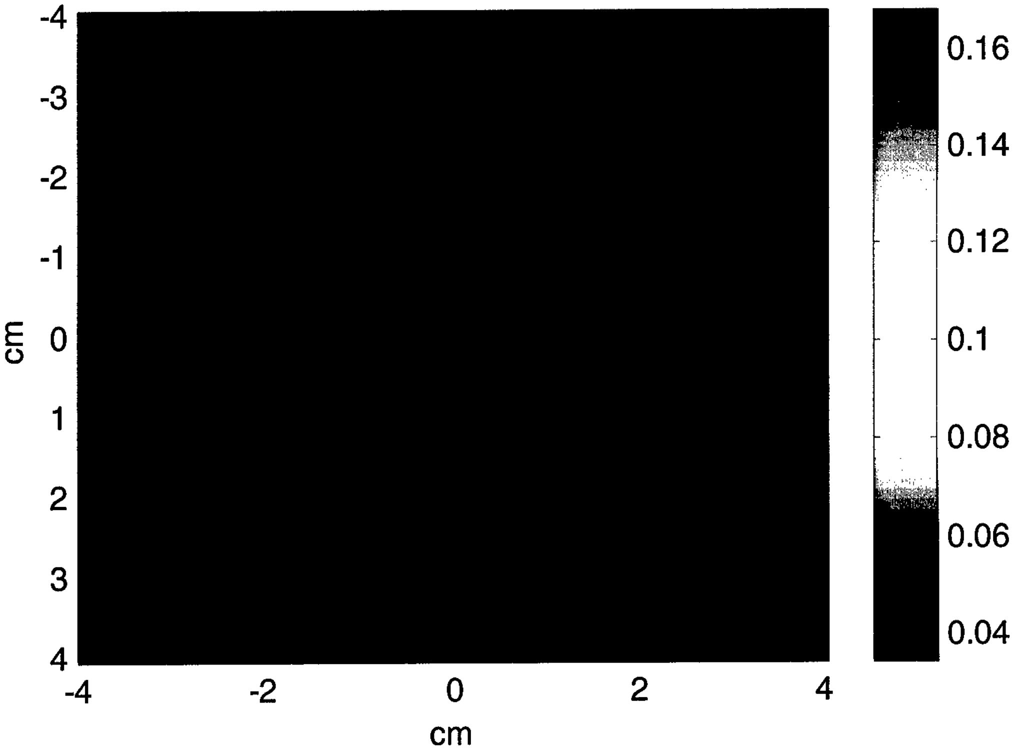

Figure 6. Absorption map obtained at 780 nm. The reconstructed absorption coefficient is 0.17 cm^{-1}.

Conclusions:

We have refined our optical imaging system and implemented imaging software. We have also optimized our combined probe by studying the optical and ultrasound sensor distributions. The combined method has been evaluated with phantoms and excised tumors and the improvement of the method compared with optical or ultrasound alone is significant.

We will start our first group of clinical study soon after we recruit several patients and we look forward to reporting our clinical results in the near future.

References:

[1] B. Tromberg, N. shah, R. Lanning, A. Cerussi, J. Espinoza, T. Pham, L. Svaasand and J. Butler, “Non-Invasive in vivo characterization of breast tumors using photon migration spectroscopy,” Neoplasia vol.2, No 1:2, pp26-40, 2000.
[2] Yodh A and Chance B,"Spectroscopy and imaging with diffusing light," Physics Today, March 1995
[3] S. Fantini, S. Walker, M. Franceschini, M. Kaschke, P. Schlag, and K. Moesta, “Assessment of the size, position, and optical properties of breast tumors in vivo by noninvasive optical methods,” App. Optics, 37: 1982:1989, (1998).
[4] S, Zhou , Y. Chen, Q. Nioka, X. Li, L. Pfaff, C.M. Cowan, and B. Chance, “A portable dual wavelength amplitude cancellation image system for the determination of human breast tumor,” SPIE Proceedings of Optical Tomography and Spectroscopy of Tissue III, 3597, 571-579, (1999).

[5] Vaupel P., "Oxygen Transport in Tumors,", in Oxygen Transport to Tissue XVII, Edited by Ince et al., Plenum Press, New York, 1996.

[6] Beauvoit B, T. Kitai, and Chance B,"Contribution of the Mitochondrial compartment to the optical properties of the rat liver," Biophysical J., Vol 67, pp. 2501-2510,1994.

[7] Folkman J," Introduction: angiogenesis and cancer," Cancer Biology 1992; 3:47-71.

[8] O'Leary, M. A., Boas, D. A., Chance, B. and Yodh, A. G "Scattering of diffuse photon density waves by spherical heterogeneities with turbid media: analytic solution and applications," Proc. Natl. Acad. Sci. USA 91, 4887-4891

[9] Y. Yao, Y. Wang, Y. Pei, W. Zhu, and RL. Barbour, "Frequency-domain optical imaging of absorption and scattering distributions by a Born iterative method," J. Opt. Soc. Am. A **14**:325-341 (1997).

[10] K. Paulsen and H. Jiang,"Spatially varing optical property reconstruction using a finite element diffusion equation approximation," Med. Phy. 22(6), June 1995.

[11] G. Rahbar, A. C. Sie, G.C. Hansen, J. S. Prince, M. L. Melany, H. Reynolds, V. P. Jackson, J. W. Sayre and L. W. Bassett, " Benign verse malignant solid breast masses: US differentiation," Radiology **213**, 889-894 (1999).

[12] V. P. Jackson , "The current role of ultrasonography in breast imaging," Radiol Clin North Am **33**, 1161-1170 (1995).

[12] F.M. Hall, J.M. Storella, D.Z. Silverstone, et al.,"Non-palpable breast lesions:recommendations for biopsy based on suspicious carcinoma of mammography," Radiology 167,pp.353-358 (1988).

[13] Stavros TA, Thickman D, Rapp C, "Solid breast nodules: Use of sonography to distinguish between benign and malignant lesions," Radiology 1995; 196: 123-134.

[14] Zhu, Q., Conant E. and Chance B., ''Optical imaging as an adjunct to sonograph in differentiating benign from malignant breast lesions," Journal of Biomedical Optics, Vol.5, No2., 229-236, April 2000.

[15] Zhu, Q., Dunrana, T., Holboke, M., Ntziachristos, V. and Yodh, A.,"A imager that combines near infrared diffusive light and ultrasound," Optics letters, (24) No.15, Aug. 1, 1999.

[16] Zhu, Q, Chen, NG, Piao DQ, Guo, P and Ding, XH , "Design of near infrared imaging probe with the assistance of ultrasound localization," July 1, Applied Optics.

[17] Chen, NG, Guo, PY, Yan, SK, Piao DQ, and **Zhu, Q**., "Simultaneous near infrared diffusive light and ultrasound imaging," Accepted by Applied Optics (June 2001).

Appendices:

Zhu, Q, Chen, NG, Ding, XH, Piao DQ, and Guo, PY, "Design of near infrared imaging probe with the assistance of ultrasound localization," Applied Optics, July, Vol. 40, No. 19, 3288-3303, 2001.

Chen, NG, Guo, PY, Yan, SK, Piao DQ, and Zhu, Q., "Simultaneous near infrared diffusive light and ultrasound imaging," Applied Optics, Accepted (July 2001).

List of presentations related to this project

Zhu, Q. Chen, NG, Guo, PY, Yan, SK, Piao, DQ "Near infrared imaging probe design with ultrasound guidance," SPIE Proc., Vol. 4256, pp 221-232 (2001).

Chen, NG, Guo, PY, Yan, SK, Piao, DQ and Zhu, Q., "Ultrasound assisted NIR imaging for breast cancer detection," Proceedings of Optical Tomography and Spectroscopy of Tissue, SPIE Vol. 4250, pp 546-557 (2001).

Zhu, Q. Chen, NG, Guo, PY, Yan, SK, "Medical Ultrasound with Simultaneous Dual-band Near-Infrared Diffusive Light Imaging and Co-registration," Proceedings of 4th Annual Conference on Information Fusion, WeC319:24 (2001).

Chen, NG. and Zhu, Q, "Optical tomography with early arriving photons: sensitivity and resolution analysis," Proceedings of Optical Tomography and Spectroscopy of Tissue, SPIE Vol. 4250, pp37-44, (2001).

Guo, PY, Yan, SK and Zhu, Q., "The design of a 1.75-D 1280-channel ultrasound imaging system," Proceedings of the IEEE27th Northeast Bioengineering Conference, pp 49-52, 2001.

Yan, SK, Guo, PY and Zhu, Q.,"Beamforming scheme and parameter tradeoff in a 1.75D ultrasound array design, Proceedings of the IEEE27th Northeast Bioengineering Conference, pp 61-62, 2001.

N. G. Chen, and Q. Zhu, "Novel Image Reconstruction Algorithm for NIR Diffusive Tomography," Proceedings of the IEEE 27th Annual Northeast Bioengineering Conference, pp 43-44 (2001)

M. Huang, P. Guo, N. G. Chen, and Quing Zhu, "Preliminary experiment results of 1.75D ultrasound array," Proceedings of the IEEE 27th Annual Northeast Bioengineering Conference, pp 51-52 (2001).

Design of near-infrared imaging probe with the assistance of ultrasound localization

Quing Zhu, Nan Guang Chen, Daqing Piao, Puyun Guo, and XiaoHui Ding

A total of 364 optical source–detector pairs were deployed uniformly over a 9 cm × 9 cm probe area initially, and then the total pairs were reduced gradually to 60 in experimental and simulation studies. For each source–detector configuration, three-dimensional (3-D) images of a 1-cm-diameter absorber of different contrasts were reconstructed from the measurements made with a frequency-domain system. The results have shown that more than 160 source–detector pairs are needed to reconstruct the absorption coefficient to within 60% of the true value and appropriate spatial and contrast resolution. However, the error in target depth estimated from 3-D images was more than 1 cm in all source–detector configurations. With the *a priori* target depth information provided by ultrasound, the accuracy of the reconstructed absorption coefficient was improved by 15% and 30% on average, and the beam width was improved by 24% and 41% on average for high- and low-contrast cases, respectively. The speed of reconstruction was improved by ten times on average. © 2001 Optical Society of America

OCIS codes: 170.0170, 170.3010, 170.5270, 170.7170, 170.3830.

1. Introduction

Recently, optical imaging techniques based on diffusive near-infrared (NIR) light have been employed to obtain interior optical properties of human tissues.[1–8] Functional imaging with NIR light has the potential to detect and diagnose diseases or cancers through the determination of hemoglobin concentration, blood O$_2$ saturation, tissue light scattering, water concentration, and the concentration and lifetime of exogenous contrast agents. Optical imaging requires that an array of sources and detectors be distributed directly or coupled through optical fibers on a boundary surface. Measurements made at all source–detector positions can be used in tomographic image reconstruction schemes to determine optical properties of the medium. The frequently used geometric configurations of sources and detectors are ring arrays[4,9–11] and planar arrays.[3,12–15] A ring array consists of multiple sources and detectors that can be distributed uniformly on a ring. Optical properties of the thin tissue slice (two-dimensional slice) enclosed by the ring can be determined from all measurements. A planar array can be configured with either transmission or reflection geometries. In transmission geometry, multiple detectors can be deployed on a planar array, and multiple sources or a single source can be deployed on an opposite plane parallel to the detector plane. Optical properties of the three-dimensional (3-D) tissue volume between the source and the detector planes can be determined from all measurements. In reflection geometry, multiple sources and detectors can be distributed on a planar probe that can be hand-held.[3,15] Optical properties of the 3-D tissue volume at slice depths below the probe can be determined from all measurements. The reflection probe configuration is desirable for the imaging of brain and breast tissues.

Although many researchers in the field have constructed imaging probes using reflection geometry,[2,3,15] to our knowledge the required total number of source–detector pairs over a given probe area needed to accurately reconstruct optical properties and localized spatial and depth distributions has not been addressed before. In this paper we study the relationship between the total number of source-detector pairs and the reconstructed imaging quality through experimental measurements. Computer simulations are performed to assist in understanding the experimental results.

Because the target localization from diffusive waves is difficult, our group and others have introduced use of *a priori* target location information pro-

---

The authors are with the Department of Electrical and Computer Engineering, University of Connecticut, 260 Glenbrook Road, U157, Storrs, Connecticut 06269. Q. Zhu's e-mail address is zhu@engr.uconn.edu.

Received 20 September 2000; revised manuscript received 21 March 2001.

0003-6935/01/193288-16$15.00/0

© 2001 Optical Society of America

vided by ultrasound to improve optical imaging.[15–18] In this paper we demonstrate experimentally that the accurate target depth information can significantly improve the accuracy of the reconstructed absorption coefficient and the reconstruction speed for any optical array configuration.

The required total number of source–detector pairs is also related to the image reconstruction algorithms used. In this paper we obtained experimental measurements using a frequency-domain system with the source amplitude modulated at 140 MHz. In simulations, forward measurements were generated by use of the analytic solution of a photon density wave scattered by a spherical inhomogeneity embedded in a semi-infinite scattering medium.[19] In both experiments and simulations, linear perturbation theory within the Born approximation was used to relate optical signals at the probe surface to absorption variations in each volume element within the sample. The total least-squares (TLS) method[20–22] was used to formulate the inverse problem. The conjugate gradient technique was employed to iteratively solve the inverse problem. Therefore the results we obtained are directly relevant to the probe design with reconstruction algorithms based on the linear perturbation theory and can be used as a first-order approximation if high-order perturbations are employed in image reconstructions.

This paper is organized as follows. In Section 2 we describe an analytic solution used to generate simulated forward data, the Born approximation, and the TLS method for image reconstruction. In Section 3 we discuss the probe geometry, a frequency-domain NIR system used to acquire the experimental measurements, and an ultrasound subsystem used to acquire the target depth information, computation procedures used to obtain both simulated and experimental absorption images. In Sections 4 and 5 we report experimental results obtained from the dense and sparse arrays with and without *a priori* target depth information. A high-contrast example is given in Section 4, and a low-contrast case is given in Section 5. Simulations are performed to assist in understanding the noise on the image reconstruction. Imaging parameters evaluated are a −6-dB width of the image lobe, the reconstructed maximum value of the absorption coefficient and its spatial location, and the image artifact level. In Sections 6 and 7 we provide a discussion and summary, respectively.

2. Basic Principles

A. Forward Model

In our experiments, forward measurements were made with a frequency-domain system operating at a 140-MHz modulation frequency. In computer simulations, forward measurements were generated from an analytic solution of a photon density wave scattered by a spherical inhomogeneity.[19] When the center of the sphere coincides with the origin of spherical coordinates, the solution for the scattered photon density wave U_{sc} outside the sphere at a detector position $\mathbf{r} = (r,\theta,\phi)$ is of the form

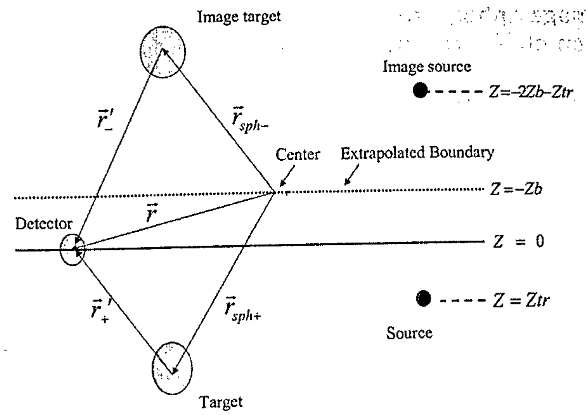

Fig. 1. Target, source, and detector configurations for a semi-infinite medium.

$$U_{\mathrm{sc}}(\mathbf{r},\omega) = \sum_{l,m} \{A_{l,m}[j_l(k^{\mathrm{out}}r) + jn_l(k^{\mathrm{out}}r)]Y_{l,m}(\theta,\phi)\}, \tag{1}$$

where j_l and n_l are spherical Bessel and Neuman functions, respectively; $Y_{l,m}(\theta,\phi)$ are the spherical harmonics, and $k^{\mathrm{out}} = [(-\nu\mu_a{}^{\mathrm{out}} + j\omega)/D^{\mathrm{out}}]^{1/2}$ is the complex wave number outside the sphere. ω is the angular modulation frequency of the light source, $\mu_a{}^{\mathrm{out}}$ is the absorption coefficient outside the sphere, and D^{out} is the photon diffusion coefficient outside the sphere given by $D^{\mathrm{out}} = 1/(3\mu_s')$, where μ_s' is the reduced scattering coefficient outside the sphere. The coefficients $A_{l,m}$, determined by the boundary conditions, are

$$A_{l,m} = -(j\upsilon Sk^{\mathrm{out}}/D^{\mathrm{out}})h_l^{(1)}(k^{\mathrm{out}}r_s)Y_{l,m}{}^*(\theta_s,\phi_s) \times \frac{D^{\mathrm{out}}xj_l(y)j_l'(x) - D^{\mathrm{in}}yj_l'(y)j_l(x)}{D^{\mathrm{out}}xh_l^{(1)\prime}(x)j_l(y) - D^{\mathrm{in}}yh_l^{(1)}(x)j_l'(y)}, \tag{2}$$

where $x = k^{\mathrm{out}}a$, $y = k^{\mathrm{in}}a$, $\mathbf{r}_s = (r_s,\theta_s,\phi_s)$ is the source position, $h_l^{(1)}$ are the Hankel functions of the first kind, and j_l' and $h_l^{(1)\prime}$ are the first derivatives of j_l and $h_l^{(1)}$. The analytic solution has the important advantage in that it is exact to all orders of perturbation theory and thus can represent accurate measurements.

We generalized the above analytic solution to a semi-infinite geometry by using a method of images with extrapolated boundary conditions (see Fig. 1). A type I boundary condition (zero light energy density at the extrapolated boundary) is used to derive the scattered wave U_{sc}'. To calculate the U_{sc}' in semi-infinite geometry, we use $\mathbf{r}_{\mathrm{sph}+} = (r_{0+},\theta_{0+},\phi_{0+})$ and $\mathbf{r}_{\mathrm{sph}-} = (r_{0-},\theta_{0-},\phi_{0-})$ to represent the centers of the sphere and the image sphere, respectively. The vectors $\mathbf{r}_+' = \mathbf{r} - \mathbf{r}_{\mathrm{sph}+} = (r_+',\theta_+',\phi_+')$ and $\mathbf{r}_-' = \mathbf{r} - \mathbf{r}_{\mathrm{sph}-} = (r_-',\theta_-',\phi_-')$ are therefore pointing to the detector position $\mathbf{r} = (r,\theta,\phi)$ from the sphere and the image sphere, respectively. The semi-infinite solution of U_{sc}' can be approximated as

$$\begin{aligned} U_{\mathrm{sc}}'(\mathbf{r},\omega) = & \sum_{l,m} \{A_{l,m}{}^{+}[j_l(k^{\mathrm{out}}r_{+}') \\ & + jn_l(k^{\mathrm{out}}r_{+}')]Y_{l,m}(\theta_{+}',\phi_{+}')\} \\ & - \sum_{l,m} \{A_{l,m}{}^{-}[j_l(k^{\mathrm{out}}r_{+}') \\ & + jn_l(k^{\mathrm{out}}r_{+}')]Y_{l,m}(\theta_{+}',\phi_{+}')\} \\ & + \sum_{l,m} \{A_{l,m}{}^{+}[j_l(k^{\mathrm{out}}r_{-}') \\ & + jn_l(k^{\mathrm{out}}r_{-}')]Y_{l,m}(\theta_{-}', \phi_{-}')\} \\ & - \sum_{l,m} \{A_{l,m}{}^{-}[j_l(k^{\mathrm{out}}r_{-}') \\ & + jn_l(k^{\mathrm{out}}r_{-}')]Y_{l,m}(\theta_{-}',\phi_{-}')\}, \end{aligned} \qquad (3)$$

where

$$\begin{aligned} A_{l,m}{}^{+} = & -(jvSK^{\mathrm{out}}/D^{\mathrm{out}})h_l^{(1)}(k^{\mathrm{out}}r_s{}^{+})Y_{l,m}{}^{*}(\theta_s{}^{+},\phi_s{}^{+}) \\ & \times \left[\frac{D^{\mathrm{out}}xj_l(y)j_l'(x) - D^{\mathrm{in}}yj_l'(y)j_l(x)}{D^{\mathrm{out}}xh_l^{(1)\prime}(x)j_l(y) - D^{\mathrm{in}}yh_l^{(1)}(x)j_l'(y)}\right., \end{aligned} \qquad (4)$$

$$\begin{aligned} A_{l,m}{}^{-} = & -(jvSk^{\mathrm{out}}/D^{\mathrm{out}})h_l^{(1)}(k^{\mathrm{out}}r_s{}^{-})Y_{l,m}{}^{*}(\theta_s{}^{-},\phi_s{}^{-}) \\ & \times \frac{D^{\mathrm{out}}xj_l(y)j_l'(x) - D^{\mathrm{in}}yj_l'(y)j_l(x)}{D^{\mathrm{out}}xh_l^{(1)\prime}(x)j_l(y) - D^{\mathrm{in}}yh_l^{(1)}(x)j_l'(y)}. \end{aligned} \qquad (5)$$

$\mathbf{r}_s{}^{+} = (r_s{}^{+},\theta_s{}^{+},\phi_s{}^{+})$ and $\mathbf{r}_s{}^{-} = (r_s{}^{-},\theta_s{}^{-},\phi_s{}^{-})$ are the positions of the source and the image source, respectively.

The incident photon density wave at the detector position $\mathbf{r}$ has the following form[3]:

$$U_{\mathrm{inc}}(\mathbf{r},\omega) = \frac{S}{4\pi D^{\mathrm{out}}}\left[\frac{\exp(jk^{\mathrm{out}}|\mathbf{r} - \mathbf{r}_s{}^{+}|)}{|\mathbf{r} - \mathbf{r}_s{}^{+}|} - \frac{\exp(jk^{\mathrm{out}}|\mathbf{r} - \mathbf{r}_s{}^{-}|)}{|\mathbf{r} - \mathbf{r}_s{}^{-}|}\right]. \qquad (6)$$

The total photon density at detector $\mathbf{r}$ is a superposition of its incident (homogeneous) and scattered (heterogeneous) waves:

$$U(\mathbf{r},\omega) = U_{\mathrm{inc}}(\mathbf{r},\omega) + U_{\mathrm{sc}}'(\mathbf{r},\omega). \qquad (7)$$

B. Born Approximation for Reconstruction

The Born approximation was used to relate $U_{\mathrm{sc}}'(\mathbf{r},\omega)$ measured at the probe surface to absorption variations in each volume element within the sample. In the Born approximation, the scattered wave that originated from a source at $\mathbf{r}_s$ and measured at detector $\mathbf{r}_d$ can be related to the medium heterogeneity $\Delta\mu_a(\mathbf{r}_v)$ by

$$U_{\mathrm{sc}}'(\mathbf{r}_{\mathrm{d}},\mathbf{r}_s,\omega) = \int G(\mathbf{r}_v,\mathbf{r}_d,\omega)U_{\mathrm{inc}}(\mathbf{r}_v,\mathbf{r}_s,\omega) \times [v\Delta\mu_a(\mathbf{r}_v)/\bar{D}]\mathrm{d}r_v{}^3, \qquad (8)$$

where $G(\mathbf{r}_v,\mathbf{r}_d,\omega)$ is the Green function and $\Delta\mu_a(\mathbf{r}_v) = \mu_a(\mathbf{r}_v) - \bar{\mu}_a$ is the medium absorption variation.[11] $\bar{\mu}_a$ is the average value of the medium absorption coefficient. By breaking the medium into discrete voxels, we obtain the following linear equations:

$$U_{\mathrm{sc}}'(\mathbf{r}_{\mathrm{di}},\mathbf{r}_{\mathrm{si}},\omega) = \sum_j^N G(\mathbf{r}_{\mathrm{vj}},\mathbf{r}_{\mathrm{di}},\omega)U_{\mathrm{inc}}(\mathbf{r}_{\mathrm{vj}},\mathbf{r}_{\mathrm{si}},\omega) \times [v\Delta\mu_a(\mathbf{r}_{vj})/\bar{D}]\Delta r_v{}^3. \qquad (9)$$

When $W_{ij} = G(\mathbf{r}_{vj},\mathbf{r}_{\mathrm{di}},\omega)\mathrm{U}_{\mathrm{inc}}(\mathbf{r}_{vj},\mathbf{r}_{\mathrm{si}},\omega)v\Delta r_v{}^3/\bar{D}$, we obtain the matrix equation of Eq. (9):

$$[W]_{MXN}\{\Delta\mu_a\}_{NX1} = [U_{\mathrm{sd}}]_{MX1}. \qquad (10)$$

The realistic constrains on $\Delta\mu_a$ are $(-\alpha \times \text{background } \mu_a) = < \Delta\mu_a < 1$, where $0 < \alpha < 1$.

The above constrains ensure that the reconstructed absorption coefficient $\hat{\mu}_a = \text{background } \mu_a + \Delta\mu_a$ is positive and not unrealistically higher than unity. With M measurements obtained from all possible source–detector pairs in the planar array, we can solve N unknowns of $\Delta\mu_a$ by inverting the matrix Eq. (10). In general, the perturbation in Eq. (10) is underdetermined ($M < N$) and ill-posed.

When the target depth is available from ultrasound, we can set $\Delta\mu_a$ of a nontarget depth equal to zero. This implies that all the measured perturbations were originated from the particular depth that contained the target. Because the number of unknowns was reduced significantly, the reconstruction converged fast.

C. Total Least-Squares Solution

To solve the unknown optical properties of Eq. (10), several iterative algorithms have been used in the literature including the regularized least-squares method[10] and the TLS method.[20,21] The TLS performs better than the regularized least-squares method when the measurement data are subject to noise and the linear operator W contains errors. The operator errors can result from both the approximations used to derive the linear model and the numerical errors in the computation of the operator. We found that the TLS method provides more accurate reconstructed optical properties than the regularized least-squares method, so we adapted the TLS method to solve the inverse problems. It has been shown by Golub[22] that the TLS minimization is equivalent to the following minimization problem:

$$\min \frac{\|U_{\mathrm{sd}} - WX\|^2}{\|X\|^2 + 1}, \qquad (11)$$

where X represents unknown optical properties. The conjugate gradient technique was employed to iteratively solve Eq. (11).

3. Methods

A. Probe Design and Imaging Geometry

There are two basic requirements to guide the design of the NIR probe. First, all source–detector separa-

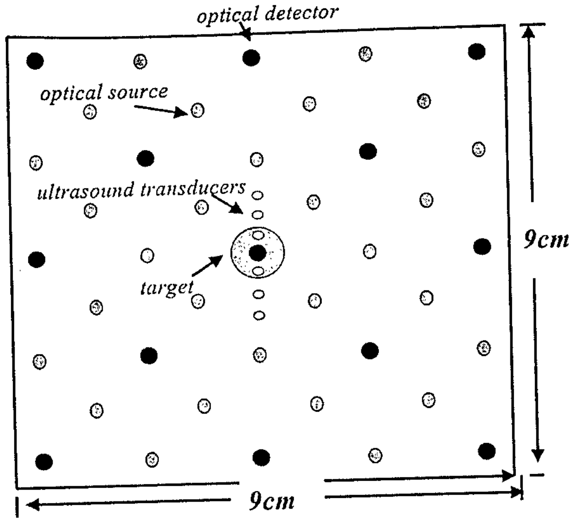

Fig. 2. Configuration of a dense array with 28 optical sources and 13 detectors as well as six ultrasound transducers. Large black circles are optical detectors, gray circles are optical sources, and small white circles are ultrasound transducers. A 1-cm-diameter spherical target was located at various depths in simulations and experiments.

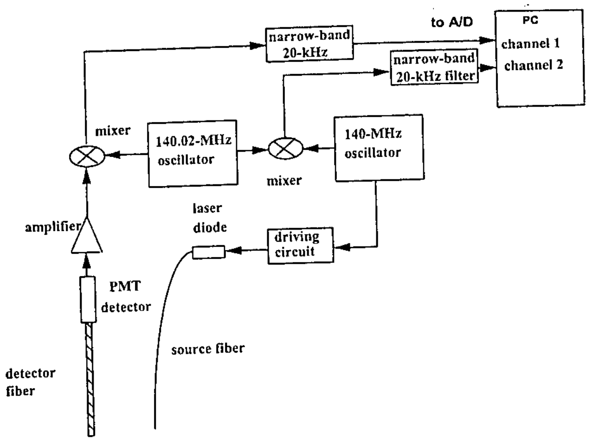

Fig. 3. Schematic of a single-channel optical data-acquisition system. A 140.02-MHz oscillator is used to drive the laser diode (780 nm) that delivers the light to the medium through the fiber. The detected signals are amplified and mixed with signals from a 140-MHz oscillator. The heterodyned 20-kHz signals are amplified, filtered, and digitized. The signals from two oscillators are also directly mixed to provide reference signals. The amplitude and phase of the waveform received through the medium are calculated from signals measured through the medium and the reference. PMT, photomultiplier tube.

tions have to be as large as 1 cm so that diffusion theory is a valid approximation for image reconstruction. Second, because the depth of a photon path is measured approximately one third to one half the source–detector separation, the distribution of source-detector distances should be from approximately 1 to 10 cm to effectively probe the depth from approximately 0.5 to 4 cm. On the basis of these requirements, we deployed a total of 28 sources and 13 detectors over a probe area of 9 cm × 9 cm (see Fig. 2). The minimum source–detector separation in the configuration is 1.4 cm and the maximum is 10.0 cm. We call this array a filled or dense array (a term adapted from ultrasound array design). The 9 cm × 9 cm × 4 cm imaging volume was discretized into voxels of size 0.5 cm × 0.5 cm × 1 cm; therefore a total of four layers in depth was obtained. The target was a 1-cm-diameter sphere located at different locations. Because one of the objectives of this study was to evaluate the target depth distribution, the centers of the four layers in depth were adapted to the target depth. For example, if the target depth was $z = 3$ cm, the centers of the four layers were chosen as 1, 2, 3, and 4 cm, respectively.

The ultrasound transducers shown in Fig. 2 were deployed simultaneously on the same probe. The diameter of each ultrasound transducer is 1.5 mm and the spacing between the transducers is 4 mm, except the two located closer to the optical detector in the middle. The spacing between these two transducers is 8 mm. Because this study requires accurate target location as a reference to compare with the reconstructed absorption image location, six transducers are used to guide the spatial positioning of a target. The target is centered when the two middle ultrasound transducers receive the strongest signals. The target depth is determined from returned pulse-echo signals. In this study we do not intend to provide ultrasound images of the target with such a sparse ultrasound array, but we demonstrate the feasibility of using *a priori* depth information to improve optical reconstruction.

In regard to the image voxel size, there is a trade-off between the accurate estimation of the weight matrix W and the voxel size. Because W_{ij} is a discrete approximation of the integral

$$\int_{v} G(\mathbf{r}_{v},\mathbf{r}_{d},\omega)U_{\mathrm{inc}}(\mathbf{r}_{v},\mathbf{r}_{s},\omega)(\nu/\bar{D})\mathrm{d}\mathbf{r}_{v}^{3},$$

it is more accurate when the voxel size is smaller. However, the total number of reconstructed unknowns will increase dramatically with the decreasing voxel size. Because the rank of the matrix W is less than or equal to the total number of measurements [Eq. (10)], a further decrease in voxel size will not add more independent information to the weight matrix. We found that a 0.5 cm × 0.5 cm × 1 cm voxel size is a good compromise. Therefore we used this voxel size in image reconstructions reported in this paper.

B. Experimental System

We constructed a NIR frequency-domain system, and the block diagram of the system is shown in Fig. 3. On the source side, a 140.000-MHz sine-wave oscillator was used to modulate the output of a 780-nm diode laser that was housed in an optical coupler (OZ Optics Inc.). The output of the diode was coupled to the turbid medium through a single 200-μm multimode optic fiber. On the reception side, an optical fiber of 3 mm in diameter was used to couple the detected light to a photomultiplier tube detector. The output of the photomultiplier tube was amplified and then mixed with a local oscillator at a frequency of 140.020 MHz. The heterodyned signal at 20 kHz after the mixer was further amplified and filtered by a bandpass filter. The outputs of two oscillators (140.000- and 140.020-MHz signals) were directly mixed to produce 20-kHz reference signals. Both signals were sampled simultaneously by a dual-channel 1.25-MHz analog-to-digital converter (A/D) board. The Hilbert transform was performed on both sampled and reference waveforms. The amplitude of the Hilbert transform of the sampled waveform corresponds to the measured amplitude, and the phase difference between the phases of the Hilbert transforms of the sampled and reference waveforms corresponds to the measured phase.

A black probe with holes shown in Fig. 2 was used to emulate the semi-infinite boundary condition. Two 3-D positioners were moved independently to position the source and detector fibers at the desired spatial locations within the 9 cm × 9 cm area.

A challenge in the reflection NIR probe design is to preserve a huge dynamic range in received signals. For example, the amplitude at a 1-cm source–detector separation measured from 0.6% Intralipid in reflection mode is approximately 84 dB larger than that at a 9-cm separation. So the signals can be saturated when they are measured from closer source–detector pairs, but they may be too low at more distant source-detector pairs. The problem can be overcome by means of controlling the light illumination. At least two illumination conditions need to be used: a low source level for closer source–detector pairs and a high level for distance source–detector pairs. In our system, a 30-dB attenuator connected to the 140-MHz oscillator was switched on and off to provide two different source levels and thus to preserve the dynamic range. Figure 4(a) shows a plot of the measured log $[\rho^2 U_{\text{sd}}(\rho)]$ versus the source–detector separation ρ, and Fig. 4(b) shows the plot of the measured phase versus the source–detector separation. The Intralipid concentration was 0.6%, which corresponded to $\mu_s{}' = 6\ \text{cm}^{-1}$. Theoretically both log $[\rho^2 U_{\text{sd}}(\rho)]$ and phase are linearly related to the source–detector separation because of the semi-infinite boundary condition used,[3] and experimental measurements shown in Fig. 4 validate that they are linearly related to the source–detector separation.

The ultrasound system consists of six transducers (see Fig. 5), a pulser (Panametrics Inc.), an A/D converter, and a multiplexer. The pulser provided a high-voltage pulse of 6-MHz central frequency to drive each selected transducer. The returned signals were received by the same transducer, amplified by the receiving circuit inside the pulser, and sampled by the A/D converter with a 100-MHz sampling frequency.

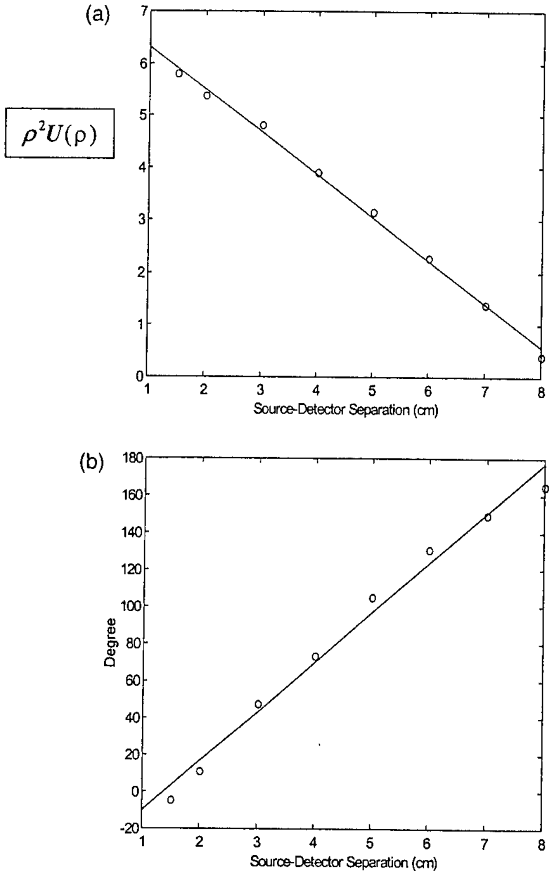

Fig. 4. Calibration curves. (a) log $[\rho^2 U(\rho)]$ versus source-detector separation. (b) Phase versus source–detector separation.

C. Computation Procedures

1. Computation Procedures of Experimental Data

To study the relationship between the total number of source–detector pairs and distributions of reconstructed optical absorption coefficients, we started from the dense array with a total of 28 sources and 13 detectors (see Fig. 2) and gradually reduced this number to generate sparse arrays with 24 × 13 (24 sources and 13 detectors), 20 × 13, 28 × 9, 24 × 9, 16 × 13, 20 × 9, 12 × 13, 16 × 9, 28 × 5, 24 × 5, 12 × 9, 20 × 5, 16 × 5, and 12 × 5 source–detector pairs, respectively. Each sparse array was a subset of the

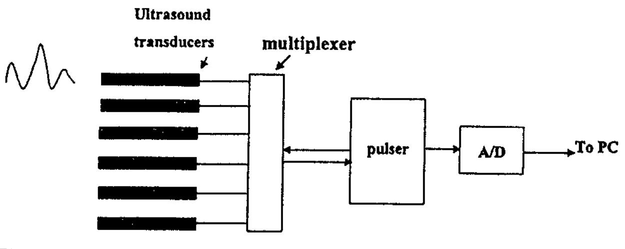

Fig. 5. Ultrasound data-acquisition system. The pulser is used to generate high-voltage pulses that are used to excite the selected ultrasound transducer. The returned signals are received by the selected transducer and are sampled by the A/D converter.

dense array, and its probe area was the same as the dense array. For each sparse array configuration, we compared the reconstructed optical imaging parameters measured from the dense array with those from the sparse arrays. The parameters include the maximum values of reconstructed $\hat{\mu}_a$ at different layers and their spatial locations, spatial resolution and artifact level of the $\hat{\mu}_a$ image, and target depth distribution. Targets of different absorption contrasts were located at different positions inside the Intralipid. For each target case, one set of measurements with the dense array was obtained, and subsets of the measurements were used as sparse array measurements. In all experiments, the background Intralipid concentration was approximately 0.6%, and μ_s' was experimentally determined from curve fitting results. Currently, we did not reconstruct target μ_s', and we used the common μ_s' for both the background and the target.

The total number of iterations or stopping criterion was difficult to determine for experimental data. Ideally, the iteration should stop when the object function [see Eq. (11)] or the error performance surface reaches the noise floor. However, the system noise, particularly coherent noise, was difficult to estimate. In general, we found that the reconstructed values were closer to true values when the object function reached approximately 5–15% of the initial value (total energy in the measurements). However, this criterion was applicable only to reconstructions with total source–detector pairs closer to the dense array case. Therefore we used this criterion for the dense array reconstruction and used the same iteration number obtained from the dense array for the sparse arrays. Thus the iteration number is normalized to the dense array case.

2. *Computation Procedures of Simulation*

Simulations were performed to assist the understanding of the random noise on the reconstructed absorption coefficient. In simulations, Gaussian noise with different standard deviations proportional to the average value of each forward data set was added to the forward measurements. Typically, 0.5%, 1.5%, and 2.0% of the average value of each forward data set were used as standard deviations to generate noise. In simulations, the target μ_a was changed to different contrast values, and target μ_s' was kept the same as the background. The background μ_a and μ_s' were 0.02 and 6 cm^{-1}, respectively.

The stopping criterion used in the simulations was based on the noise level of the object function. Considering that the object function fluctuates within one standard deviation σ around the mean E when the iteration number is large, we can use $E + \sigma$ as a stopping criterion, i.e., the iteration will stop if the object function is less than $E + \sigma$. When the linear perturbation is assumed, E can be approximated as $\Sigma_j^N n(j)^2$ and σ as $\Sigma_j^N[2n(j)^4]^{1/2}$, where N is the total number of source–detector pairs and $n(j)$ is the generated random noise with a standard deviation proportional to the specified percentage of the mean of the forward data set.

D. Testing Targets

Spherical testing targets of ~1 cm in diameter were made of acrylamide gel.[16] The acrylamide powder was dissolved in distilled water, and 20% concentration of Intralipid was added to the acrylamide solution to dilute the solution to a 0.6% Intralipid concentration ($\mu_s' = 6$ cm^{-1}). India ink was added to the solution to produce target μ_a of different values. Acoustic scattering particles of 200 μm in diameter were added to the solution before polymerization. Components of ammonium persulfate and tetramethylethylenediamine (known as TEMED) were added to the solution to produce polymerization.

4. Results of a High-Contrast Target Case

A. Experimental Results of a Dense Array

Figure 6(a) is an experimental image of a high-contrast target ($\mu_a = 0.25$ cm^{-1}) located in the Intralipid background ($\mu_s' = 6$ cm^{-1}). The target was a 1-cm-diameter sphere and its center was located at ($x = 0$, $y = 0$, $z = 3.0$ cm), where x and y were the spatial coordinates and z was the propagation depth. The target depth was well controlled by use of ultrasound pulse-echo signals, and the error was less than 1 mm. The 3-D images were reconstructed from the measurements made with the dense array, and the image shown was obtained at target layer 3. The centers of the imaging voxels in z are 1, 2, 3, and 4 cm for layers 1, 2, 3, and 4, respectively. The measured maximum value of the image lobe [$\hat{\mu}_{a(\max)}$] was 0.233 cm^{-1}, which was a close estimate of the target μ_a. The measured spatial location of $\hat{\mu}_{a(\max)}$ was ($x = 0.5$ cm, $y = 0.0$ cm), which agreed reasonably well with the true target location. The spatial resolution can be estimated from the −6-dB contour plot of Fig. 6(a), which is shown in Fig. 6(b). The outer contour is −6 dB from the $\hat{\mu}_{a(\max)}$, and the contour spacing is 1 dB. The width of the image lobe measured at the −6 dB-level corresponds to a full width at half-maximum (FWHM), which is commonly used to estimate resolution. The measured widths of longer and shorter axes were 1.01 and 1.60 cm, respectively, and the geometric mean was 1.27 cm, which was used to represent the −6-dB beam width. The contrast resolution can be estimated from the peak artifact level, and no artifact was observed in the image. The target depth can be assessed from the images obtained from other nontarget layers. Figure 6(c) is the image obtained at nontarget layer 4, and an image lobe of $\hat{\mu}_{a(\max)} = 0.138$ cm^{-1} was observed. The spatial location of $\hat{\mu}_{a(\max)}$ was ($x = 0.0$, $y = 0.0$), which agreed well with the true target location. No distinct lobes were observed at nontarget layers 1 and 2, which indicates that the error in the target depth estimated from 3-D images was approximately 1 cm. Because the error in the true target depth was less

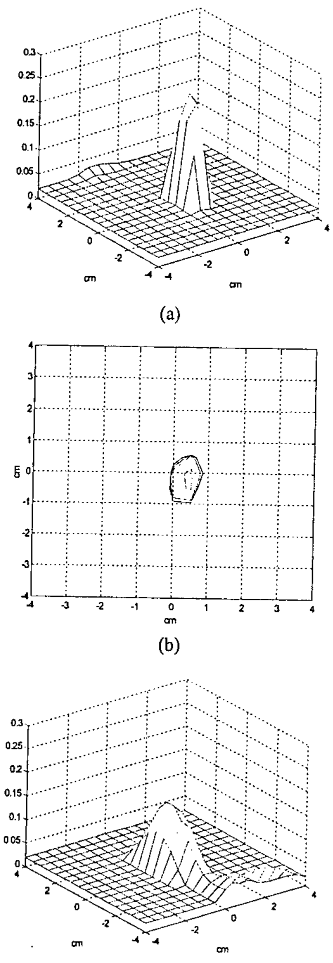

(a)

(b)

(c)

Fig. 6. Experimental 3-D images of $\hat{\mu}_a$ reconstructed with a total of $28 \times 13 = 364$ source–detector pairs at 2437 iterations. The target ($\mu_a = 0.25\ \text{cm}^{-1}$) was located at ($x = 0, y = 0, z = 3.0$ cm) inside the Intralipid background. (a) Reconstructed $\hat{\mu}_a$ at target layer 3. The horizontal axes represent spatial x and y coordinates in centimeters, and the vertical axis is the $\hat{\mu}_a$. The measured maximum value of the image lobe [$\hat{\mu}_{a(\max)}$] was $0.233\ \text{cm}^{-1}$, and its location was ($x = 0.5, y = 0.0$). No image artifacts were observed. (b) −6-dB contour plot of (a). The outer contour is −6 dB from the $\hat{\mu}_{a(\max)}$, and the contour spacing is 1 dB. The measured −6-dB beam width was 1.27 cm. (c) Reconstructed $\hat{\mu}_a$ at nontarget layer 4. An image lobe of strength $0.138\ \text{cm}^{-1}$ and spatial location of ($x = 0.0, y = 0.0$) was observed.

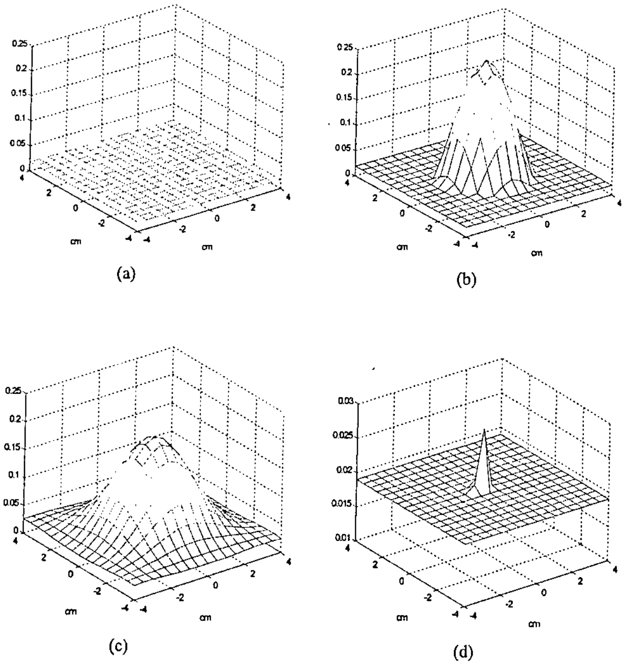

(a) (b)

(c) (d)

Fig. 7. Simulated 3-D images of $\hat{\mu}_a$ reconstructed with a total of $28 \times 13 = 364$ source–detector pairs. The target ($\mu_a = 0.25\ \text{cm}^{-1}$) was located at ($x = 0, y = 0, z = 3.0$ cm) inside the Intralipid background. (a) Reconstructed $\hat{\mu}_a$ at nontarget layer 2 (simulation, 0.5% noise). No image lobe was observed. (b) Reconstructed $\hat{\mu}_a$ at target layer 3 (simulation, 0.5% noise). The target of strength $\hat{\mu}_{a(\max)} = 0.248\ \text{cm}^{-1}$ and the spatial location (0.0, 0.0) was observed. (c) Reconstructed $\hat{\mu}_a$ at nontarget layer 4 (simulation, 0.5% noise). The target of strength $0.190\ \text{cm}^{-1}$ and location ($x = 0.0, y = 0.0$) was observed. (d). Reconstructed $\hat{\mu}_a$ at nontarget layer 2 with 1.0% noise. The target of $0.028\ \text{cm}^{-1}$ was observed. Note that the scale of (d) is different from (a)–(c).

than 1 mm, this 1-cm error was due largely to the depth uncertainty of diffusive waves.

B. Simulation Results of a Dense Array

Our simulations support the experimental results. Figure 7 shows simulation results obtained with the dense array. A simulated 1-cm-diameter absorber ($\mu_a = 0.25\ \text{cm}^{-1}$) was located at ($x = 0, y = 0, z = 3$ cm) inside a homogeneous scattering background ($\mu_s' = 6\ \text{cm}^{-1}$). We added 0.5% Gaussian noise to the forward data generated from the analytic solution. Images obtained at nontarget layer 2, target layer 3, and nontarget layer 4 are shown in Fig. 7(a), Fig. (b), and 7(c), respectively. No target was found at layer 2, and the target of strengths 0.248 and $0.190\ \text{cm}^{-1}$ appeared at layers 3 and 4, respectively. However, when the noise level in the forward data was increased to 1.0%, the target of strength $\hat{\mu}_{a(\max)} = 0.028\ \text{cm}^{-1}$ appeared at nontarget layer 2 [Fig. 7(d)] as well as target layer 3 [$\hat{\mu}_{a(\max)} = 0.163\ \text{cm}^{-1}$] and nontarget layer 4 [$\hat{\mu}_{a(\max)} = 0.111\ \text{cm}^{-1}$]. This suggests that measurement noise is an important parameter to affect the target depth estimate.

C. Experimental Results of a Dense Array with Ultrasound Assistance

From ultrasound we obtained the target depth as well as the target boundary information. Figure 8(a) shows the received pulse-echo signals (from a depth of 2.3–3.5 cm) obtained from the six ultrasound transducers (see Fig. 2). The spatial dimension covered by the six transducers is 2.4 cm. The front surface of the target was indicated clearly by the returned pulses shown by two arrows, and the back surface was seen through the reflection of a soft plastic plate. The reflected signals of the back surface are also shown by arrows. The plate was used to hold the target and was transparent to light. The measured depth of the target front surface was 2.44 cm and the back surface was 3.43 cm. The distance

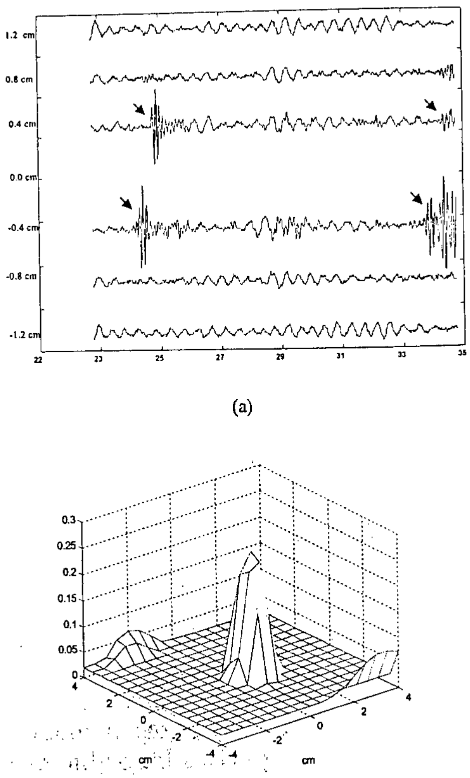

(a)

(b)

Fig. 8. (a) Ultrasound pulse-echo signals or *A*-scan lines obtained from six transducers. The abscissa is the propagation depth in millimeters. From reflected signals, the measured depth of the target front surface is 2.44 cm, and the back surface is 3.43 cm. The center of the target is ~3 cm. The total length of the signal corresponds to 1.2 cm in depth, and the measured distance between the front and the back surfaces is 0.993 cm. The spatial dimension covered by the transducers is 2.4 cm. (b) An image of the high-contrast target reconstructed at a target layer when we used only *a priori* target depth information provided by ultrasound. The reconstructed $\hat{\mu}_{a(\max)}$ reached 0.245 cm^{-1} at 216 iterations.

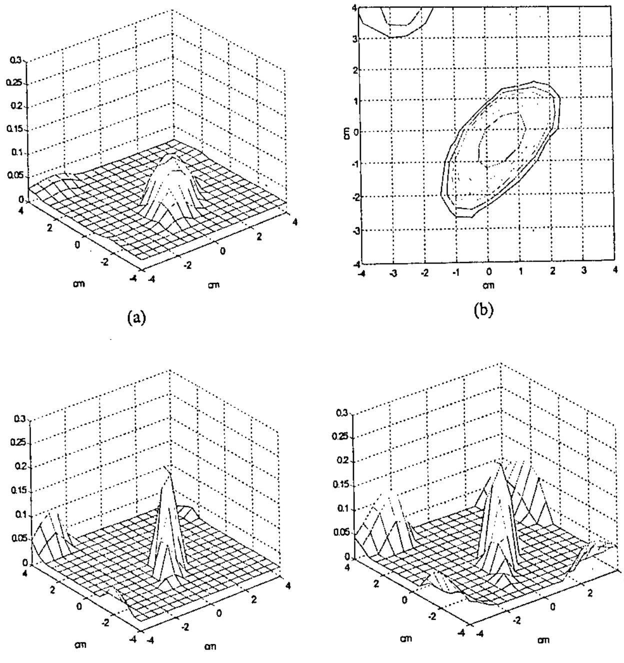

(a)

(b)

(c)

(d)

Fig. 9. Experimental images at target layer 3 reconstructed with a total of $16 \times 5 = 80$ source–detector pairs. (a) Reconstructed $\hat{\mu}_a$ at target layer 3 with 2478 iterations. The measured $\hat{\mu}_{a(\max)}$ was 0.107 cm^{-1}, which was 43% of the true value, and the spatial location of $\hat{\mu}_{a(\max)}$ was ($x = 0.5, y = -0.5$). The measured peak image artifact level was −10 dB below the peak of the main image lobe. (b) −12-dB contour plot of (a). The outer contour is −12 dB, and the contour spacing is 2 dB. The measured −6-dB beam width was 2.55 cm, which was 200% broader than that of the dense array. (c) Reconstructed $\hat{\mu}_a$ at target layer 3 with 10,000 iterations. The measured $\hat{\mu}_{a(\max)}$ reached 0.264 cm^{-1}, and the peak artifact level was increased by 2 dB as well. (d) Reconstructed $\hat{\mu}_a$ at the target layer with only *a priori* target depth information provided by ultrasound. $\hat{\mu}_{a(\max)} = 0.173$ cm^{-1} at 216 iterations.

between the peaks of front reflection and backreflection was 0.993 cm, which corresponded to the target size. With the assistance of target depth, we reconstructed the absorption image at the target layer only. Figure 8(b) is the reconstructed $\hat{\mu}_a$ obtained from the dense array measurements. A total of 216 iterations were used to obtain $\hat{\mu}_{a(\max)} = 0.245$ cm^{-1}, and the reconstruction was approximately ten times faster than that without the depth information. The spatial resolution was approximately the same as Fig. 6(a), and the −6-dB beam width was 1.31 cm. The contrast resolution was 5 dB poorer because the measurement noise was lumped to single-layer reconstruction instead of being distributed to four layers.

D. Experimental Results of a Sparse Array

The imaging quality of sparse arrays decreased. Figure 9(a) is an experimental image at target layer 3 obtained from the 16×5 sparse array. The sparse array measurements used were a subset of the dense array measurements. The measured $\hat{\mu}_{a(\max)}$ was 0.107 cm^{-1}, which was 43% of the true value. The −6-dB beam width was 2.55 cm, which was 200% broader than that of the dense array. Edge artifacts were observed and are best seen from Fig. 9(b), which is the −12-dB contour plot of Fig. 9(a). The outer contour is −12 dB, and the spacing is 2 dB. The peak artifact level is −10 dB from the $\hat{\mu}_{a(\max)}$. The reconstructed $\hat{\mu}_a$ can be increased if the iteration is significantly increased. The iteration number used to obtain Fig. 9(a) was 2478, which was the same as that used to obtain Fig. 6. When the iteration number was increased to 10,000 for the sparse array case, the reconstructed $\hat{\mu}_{a(\max)}$ reached 0.264 cm^{-1}, which was close to the true target μ_a. However, the image artifact level was increased too [see Fig. 9(c)], and the ratio of the peak artifact to $\hat{\mu}_{a(\max)}$ was 2 dB higher than that shown in Fig. 9(a). In addition, the background noise fluctuation of nontarget layers 1 and 2 was increased. The noise fluctuation can be estimated from the standard deviations of reconstructed $\hat{\mu}_a$ at nontarget layers 1 and 2. At 2478 iterations, the averages and the standard deviations of $\hat{\mu}_a$ were 0.0233 ($\pm$0.0028) and 0.0202 cm^{-1} ($\pm$0.0022 cm^{-1}) for nontarget layers 1 and 2, respectively, and these values were 0.0244 ($\pm$0.0078) and 0.0208 cm^{-1} ($\pm$0.0073 cm^{-1}) at 10,000 iterations.

The measured maximum values of the image lobes or target strengths at the target layer and nontarget layer 4 continuously grew with each iteration, even though the reconstructed values at the target layer were close to the true value. This problem was mentioned in the literature,[11] but was not explained well. It is largely related to use of nonlinear constrains on $\Delta\mu_a$ in Eq. (10), particularly the choice of α. When α is close to 1, the reconstruction converges fast, and the target strength increases little after a certain number of iterations. When α is close to 0, the reconstruction converges slowly, and the target strength grows continuously. However, when the measurement signal-to-noise ratio (SNR) is not high, for example, in sparse array or low-contrast cases, the choice of $\alpha \approx 1$ can cause unstable reconstruction. In some cases, the reconstructed images can jump from one set of $\hat{\mu}_a$ to another, which causes the object function to increase suddenly and reduce again. This is related to the underdetermined nature of Eq. (10), i.e., the unknowns are far more than the measurements. In some cases the reconstructed images have multiple lobes of similar strengths, which indicate that the reconstruction does not converge at all. In all cases, the image background fluctuations were large compared with the fluctuations when a smaller α was used. We found that α between 0.1 and 0.4 can provide stable reconstruction, and we used $\alpha \approx$ 0.1 for all experiments.

Another factor that accounts for the slow increase in the reconstructed value is use of linear perturbation to approximate the measurements that contain all higher-order perturbations. The minimization procedure [Eq. (11)] blindly minimizes the difference between the measurements and their linear approximation $W\Delta\mu_a$ and therefore reconstructs higher and higher $\Delta\mu_a$ if the iteration continues.

The target depth estimate was poorer than that of the dense array because of the lower SNR of the sparse array measurements. Similar to the dense array case, a target of strength $\hat{\mu}_{a(\max)} = 0.072\ \text{cm}^{-1}$ and location ($x = 0.5, y = 0.0$) was observed at nontarget layer 4. In addition, a target of strength $\hat{\mu}_{a(\max)} = 0.0348\ \text{cm}^{-1}$ and location ($x = 0.5, y = -0.5$) was observed at nontarget layer 2. However, the target mass, which was approximately the volume underneath the image lobe, was much smaller than that obtained at layers 3 and 4, and the target at layer 2 was buried in the background noise.

Figure 9(d) is the reconstructed $\hat{\mu}_a$ at the target layer from only the sparse array measurements. A total of 216 iteration steps were used to obtain $\hat{\mu}_{a(\max)} = 0.173\ \text{cm}^{-1}$, and the reconstruction was approximately 50 times faster than that without the depth information. The measured −6-dB beam width was 1.49 cm, which was approximately the same as Fig. 9(c) but was improved 42% from Fig. 9(a). The contrast resolution was 2 dB worse for the same reason discussed above.

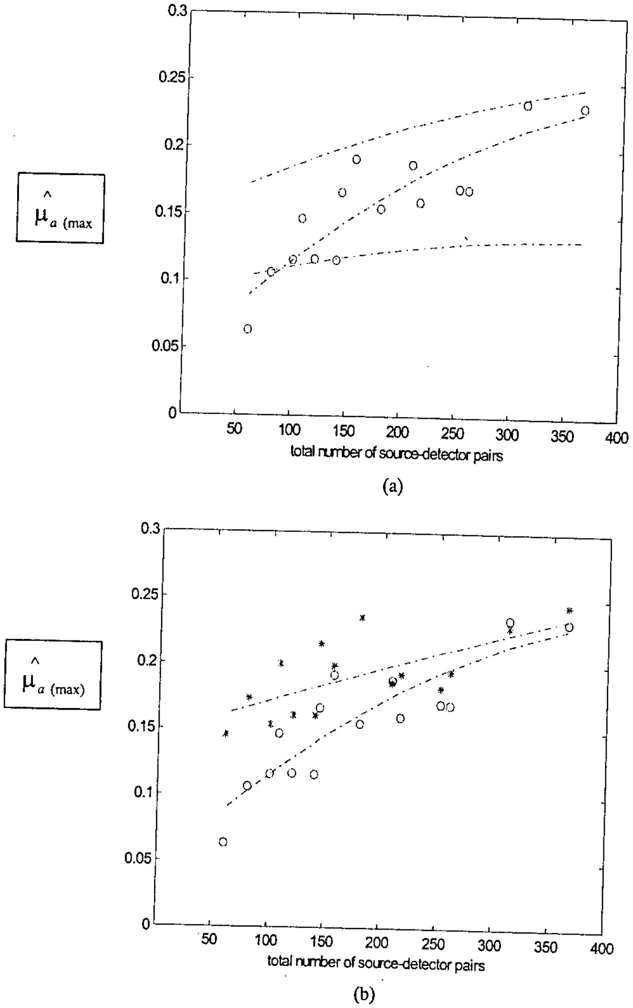

(a)

(b)

Fig. 10. $\hat{\mu}_{a(\max)}$ versus the total number of source–detector pairs. The center of the target ($\mu_a = 0.25\ \text{cm}^{-1}$) was located at ($x = 0.0$, $y = 0.0, z = 3.0$ cm) in computer simulations and experiments. (a) Curves were obtained at the target layer. Two dashed curves (upper and lower) are the curve-fitting results of simulation data points obtained with 0.5% and 2.0% noise added to the forward data, respectively. The experimental data are plotted with circles, and the dashed curve in the middle is the fitting result of the experimental points. (b) The measured target strength (circles) and the curve-fitting result (lower curve). The measured target strength (stars) was reconstructed at the target layer only by use of *a priori* depth information and the curve fitting result (upper curve).

E. Simulation and Experimental Results of Reconstructed $\hat{\mu}_{a(\max)}$ versus Total Number of Source–Detector Pairs

To understand the effects of random noise on the performance of the reconstruction, we performed simulations for each array configuration. Gaussian noise of 0.5%, 1.0%, 1.5%, and 2.0% were added to each forward data set generated from the analytic solution [see Eq. (3)]. The center of a simulated 1-cm-diameter spherical target ($\mu_a = 0.25$

cm^{-1}) was located at ($x = 0$, $y = 0$, $z = 3.0$ cm). Reconstructed images at different noise levels were obtained for each array configuration, and the peak values of image lobes [$\hat{\mu}_{a(\max)}$] at target layer 3 were measured. Figure 10(a) shows simulation and experimental results of reconstructed $\hat{\mu}_{a(\max)}$ versus the total number of source–detector pairs. Two dashed curves are the fitting results of simulated data points with 0.5% (upper) and 2.0% (lower) noise. The dashed curve in the middle is the fitting result of experimental points plotted with circles. Second-order polynomials were used for all curve fittings. The reduction of the reconstructed $\hat{\mu}_{a(\max)}$ was significant when the noise level went up in the simulated data. Because the SNR of experimental data was decreased when the total number of source–detector pairs was reduced, the data were scattered around the 0.5% noise curve when the total pairs were large and were distributed around the 2.0% noise curve (values were 60% less than that obtained from the dense array) when the total pairs were reduced to less than 140. However, because our experimental system has both coherent and random noise, simulations based on random noise can only qualitatively explain the noise effect on the experimental data.

Figure 10(b) shows the experimental results of reconstructed $\hat{\mu}_{a(\max)}$ versus the total number of source–detector pairs obtained from 3-D imaging (circles) and ultrasound-assisted imaging (stars). The upper curve is the fitting result of the circles, and the lower curve is the result of the stars. In both cases, the reconstructed values were decreased when the total number of pairs was reduced. However, the reconstructed values were more accurate when the target depth information was available, and the improvement on average was 15%. The improvement was more dramatic when the total pairs were less.

For sparse arrays with total source–detector pairs less than 140, the reconstructed $\hat{\mu}_{a(\max)}$ could be increased if the iterations were significantly increased. However, the image artifact level of the target layer and the noise level of the nontarget layers were increased too. With the assistance of simulations, we offer the following explanations to the increased image artifact and noise level problem. In simulations, the iteration was stopped when the TLS error between the measurement and the linear approximation reached the noise floor, which was

$$E + \sigma = \sum_{j}^{N} n(j)^2 + \sum_{j}^{N} [2n(j)^4]^{1/2},$$

where $n(j)$ was the generated random noise with the standard deviation proportional to a certain percent of the mean of the forward data set for each array configuration. When the object function reached the noise floor, the gradient

$$\nabla g = \frac{-2(U_{\text{sd}} - W\Delta\mu_a)^T(W)}{\Delta\mu_a{}^T\,\Delta\mu_a + 1} - \frac{-2(U_{\text{sc}} - W\Delta\mu_a)^T(U_{\text{sd}} - W\Delta\mu_a)(\Delta\mu_a)}{(\Delta\mu_a{}^T\,\Delta\mu_a + 1)^2}$$

can be approximated as

$$\nabla g \approx \frac{-2(N)^T(W)}{\Delta\mu_a{}^T\Delta\mu_a + 1} - \frac{-2(N)^T(N)(\Delta\mu_a)}{(\Delta\mu_a{}^T\Delta\mu_a + 1)^2},$$

where N is the noise vector. Therefore the search procedure of Eq. (11) is more random and noisy. Because $\Delta\mu_{a_{(\text{new})}} = \Delta\mu_{a_{(\text{old})}} + \beta\nabla g$, the $\Delta\mu_a$ updating is more random and noisy. β is proportional to the square of the gradient. Continuous iteration when the object function has reached the noise floor may destroy the convergence of the reconstruction. We found that when the SNR of the data is high, for example, high-contrast cases, continuous iteration in general increases reconstructed μ_a and sidelobes. However, when the SNR of the data is low, for example, low-contrast cases, continuous iteration does not increase the reconstructed μ_a, but destroys the convergence of the reconstruction [see Fig. 12(c) below].

F. Experimental Results of Imaging Parameters Versus Total Number of Source–Detector Pairs

The imaging parameters measured from different array configurations are listed in Table 1. Listed first are the measured parameters at target layer 3. These parameters are a −6-dB beam width of the image lobe, the peak sidelobe level, $\hat{\mu}_{a(\max)}$, and the distance in the x–y plane between the location of $\hat{\mu}_{a(\max)}$ and the true target location. Next are the same parameters measured at nontarget layer 4. The increase in beam width was negligible for the arrays with more than 140 source–detector pairs and was 100% broader for the sparse arrays with total pairs less than this number. The sidelobe level was progressively increased when the total pairs were reduced. At nontarget layer 4, when the total pairs were reduced to less than 140, the measured image lobes were broad and no sidelobes were seen. The agreement between the measured $\hat{\mu}_{a(\max)}$ location and the true target location is good for all the array configurations, which suggests that this parameter is not sensitive to the total number of source–detector pairs in high-contrast cases. Table 1 next lists the strength of the target measured at nontarget layer 2 and its spatial location. Because the SNR of the sparse array measurement was lower, the target appeared at layer 2 when total pairs were less than 180. However, in all cases, the target mass measured at this layer was much smaller than that obtained at the target layer and nontarget layer 4. Finally, Table 1 lists the measured imaging parameters when the target depth was available to optical reconstruction. Compared with parameters obtained from optical im-

Table 1. Imaging Parameters Measured with Different Array Configurations: High-Contrast Target Case ($\mu_a = 0.25\ \text{cm}^{-1}$)

Parameter	Total Pairs														
	28 × 13	24 × 13	20 × 13	28 × 9	24 × 9	16 × 13	20 × 9	12 × 13	16 × 9	28 × 5	24 × 5	12 × 9	20 × 5	16 × 5	12 × 5
Target layer 3 (2437 iterations)															
−6-dB beam width (cm)	1.27	1.42	1.65	1.67	1.70	1.44	1.78	1.39	1.55	*2.45*	*2.34*	*1.69*	*2.50*	*2.55*	*3.09*
Peak sidelobe (dB)	−18	−13	−12	−14	−13	−16	−12	−13	−11	−12	−11	−10	−11	−10	−8
$\hat{\mu}_{a(\max)}$ (cm^{-1})	0.23	0.23	0.17	0.17	0.16	0.18	0.16	0.19	0.17	0.12	0.12	0.15	0.12	0.11	0.06
$\lvert\hat{\mu}_{a(\max)} - (0,0)\rvert$ (cm)	0.5	0.7	0.7	0.5	0.5	0.7	0.5	0.7	0.7	0.5	0.5	0.7	0.5	0.7	0.7
Nontarget layer 4 (2437 iterations)															
−6-dB beam width (cm)	2.10	2.11	2.48	2.40	2.52	2.26	2.59	2.40	2.54	4.35	4.10	2.63	3.93	4.51	5.36
Peak sidelobe (dB)	−8	−9	−17	−14	−13	−19	−12	−13	−12						
$\hat{\mu}_{a(\max)}$ (cm^{-1})	0.14	0.14	0.12	0.11	0.11	0.14	0.11	0.14	0.13	0.06	0.07	0.12	0.06	0.07	0.07
$\lvert\hat{\mu}_{a(\max)} - (0,0)\rvert$ (cm)	0.0	0.5	0.0	0.7	0.7	0.5	0.7	0.0	0.7	0.5	0.5	0.7	0.5	0.5	0.5
Nontarget layer 2 (2437 iterations)															
$\hat{\mu}_{a(\max)}$ (cm^{-1})	0.00	0.00	0.00	0.00	0.00	0.00	0.043	0.024	0.047	0.026	0.043	0.048	0.032	0.035	0.038
$\lvert\hat{\mu}_{a(\max)} - (0,0)\rvert$ (cm)							1.12	0.70	1.12	0.70	1.00	1.12	0.70	0.70	0.5
Target layer only (216 iterations)															
−6-dB beam width (cm)	1.31	1.40	1.68	1.61	1.55	1.57	1.50	1.41	1.20	1.71	1.48	1.45	1.77	1.49	1.75
Peak sidelobe (dB)	−12	−12	−12	−9	−8	−12	−7	−9	−7	−8	−8	−6	−8	−8	−8
$\hat{\mu}_{a(\max)}$ (cm^{-1})	0.25	0.23	0.19	0.18	0.19	0.19	0.24	0.20	0.22	0.16	0.16	0.20	0.15	0.17	0.15
$\lvert\hat{\mu}_{a(\max)} - (0,0)\rvert$ (cm)	0.5	0.5	0.5	0.5	0.5	0.5	0.5	0.5	0.5	0.5	0.5	0.5	0.5	0.5	0.5

Note: Italicized entries are 100% broader than the dense array beam width.

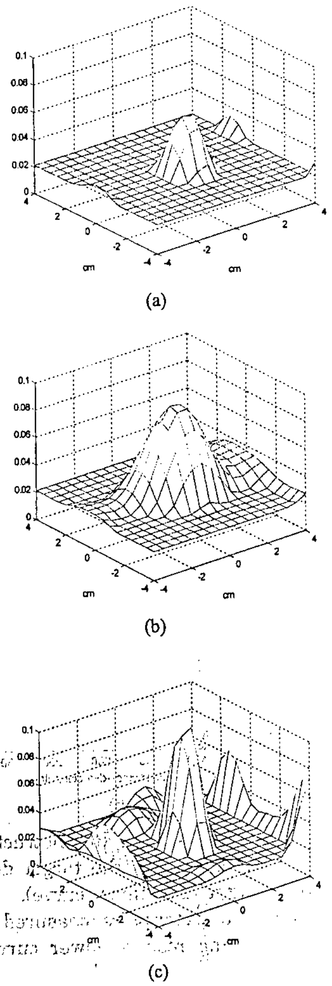

Fig. 11. Experimental images of $\hat{\mu}_a$ reconstructed from a total of $28 \times 13 = 364$ source–detector pairs. The target ($\mu_a = 0.10$ cm^{-1}) was located at ($x = 0, y = 0, z = 2.5$ cm) inside the Intralipid background. (a) Reconstructed $\hat{\mu}_a$ at target layer 3. The measured $\hat{\mu}_{a(\max)}$ was 0.063 cm^{-1} at 510 iterations, and its location was ($x = 0.0, y = -0.5$). Edge artifacts were observed and the peak level was −7 dB from the $\hat{\mu}_{a(\max)}$. (b) Reconstructed $\hat{\mu}_a$ at nontarget layer 4. The measured $\hat{\mu}_{a(\max)}$ was 0.0871 cm^{-1} at 510 iterations, and its location was ($x = 0, y = 0$). (c) Reconstructed $\hat{\mu}_a$ at the target layer when only the target depth information provided by ultrasound was used. $\hat{\mu}_{a(\max)} = 0.107$ cm^{-1} at 56 iterations.

aging only, the −6-dB beam width was improved by 24% on average, and the reconstruction speed was approximately 10 times faster; however, the sidelobe was 3 dB worse.

5. Results of a Lower-Contrast Target Case

A. Experimental Results of a Dense Array

To study the effects of target contrast on the quality of the reconstructed image for each array configuration, we conducted a set of experiments with a lower-contrast target ($\mu_a = 0.10$ cm^{-1}) embedded in the Intralipid. The center of the target was located at ($x = 0, y = 0, z = 2.5$ cm). The centers of the imaging voxels in z were 0.5, 1.5, 2.5, and 3.5 cm for layers 1, 2, 3, and 4, respectively. Figure 11 shows the images of the lower-contrast target obtained at target layer 3 [Fig. 11(a)] and deeper nontarget layer 4 [Fig. 11(b)]. The images were reconstructed from the measurements made with the dense array. At target layer 3, the measured $\hat{\mu}_{a(\max)}$ was 0.063 cm^{-1}, which was approximately 63% of the target μ_a. The measured spatial location of $\hat{\mu}_{a(\max)}$ was ($x = 0.0, y = -0.5$), which agreed reasonably well with the true target location. The measured −6-dB beam width was 1.83 cm, which was 144% times broader than the beam width of the high-contrast case. Edge artifacts were observed, and the peak level was −7 dB from the $\hat{\mu}_{a(\max)}$. At nontarget layer 4, the measured $\hat{\mu}_{a(\max)}$ was 0.0871 cm^{-1}, which was even higher than that measured at the target layer. Because the SNR of the data was lower than the high-contrast case, the target depth estimate was poorer. A target of $\hat{\mu}_{a(\max)} = 0.0543$ cm^{-1} located at ($x = 0, y = -0.5$) was observed at nontarget layer 2, and its mass was much smaller than that obtained at the target layer and nontarget layer 4.

Figure 11(c) is the reconstructed $\hat{\mu}_a$ at the target

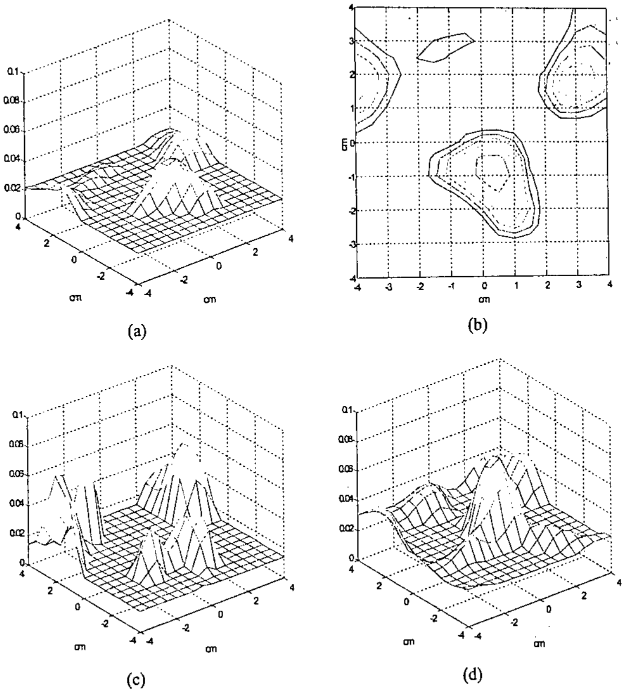

Fig. 12. Experimental images of $\hat{\mu}_a$ at target layer 3 reconstructed from a total of $24 \times 5 = 120$ source–detector pairs. (a) Reconstructed $\hat{\mu}_a$ at target layer 3 with 510 iterations. The measured $\hat{\mu}_{a(\max)}$ was 0.049 cm^{-1}, which was 49% of the true target μ_a, and its location was ($x = 0.5, y = -1.0$), which was displaced from the true target location by 1.11 cm. Image artifacts were observed, and the peak was −3 dB from the $\hat{\mu}_{a(\max)}$. (b) −6-dB contour plot of (a). (c) Reconstructed $\hat{\mu}_a$ at target layer 3 with 1500 iterations. The peak artifact was 5 dB higher than the image lobe. (d) Reconstructed $\hat{\mu}_a$ at target layer 3 (56 iterations) with only *a priori* target depth information provided by ultrasound. The measured $\hat{\mu}_{a(\max)}$ was 0.074 cm^{-1}, and its location was ($x = 0.5, y = -0.5$). Image artifacts were observed, and the peak was −5 dB from the $\hat{\mu}_{a(\max)}$.

layer from only the dense array measurements. A total of 56 iterations were used to obtain $\hat{\mu}_{a(\max)} = 0.107\ \text{cm}^{-1}$, and the reconstruction was approximately ten times faster than that without the depth information. The spatial resolution was 8% better than that obtained from Fig. 11(a), and the −6-dB beam width was 1.67 cm. The contrast resolution was 2 dB worse.

B. Experimental Results of a Sparse Array

The imaging quality of sparse arrays decreased. Figure 12(a) is an image of the same target ($\mu_a = 0.10\ \text{cm}^{-1}$) reconstructed from measurements made with the 24 × 5 sparse array. The measured $\hat{\mu}_{a(\max)}$ was $0.049\ \text{cm}^{-1}$, which was 49% of the true value. The −6-dB contour plot is shown in Fig. 12(b). The measured spatial location of $\hat{\mu}_{a(\max)}$ was ($x = 0.5$, $y = -1.0$), which was displaced from the true target location by 1.11 cm in radius. The measured −6-dB beam width was 2.98 cm, which was 163% broader than that measured from the dense array. Sidelobes were abundant, and the peak value was −3 dB below the peak of the image lobe. These sidelobes would produce false targets in the image if no *a priori* information about the target locations were given.

In this case, continuous iteration did not increase the target strength but increased the sidelobe strength. Figure 12(a) was obtained at 510 iterations, whereas Fig. 12(c) was obtained at 1500 iterations. After approximately three times more iterations, the peak of the artifact was 5 dB higher than the peak of the image lobe. The target depth estimated from 3-D images was worse at 1500 iterations than that at the 510 iterations. The measured target strengths at nontarget layer 2 were 0.064 and $0.1661\ \text{cm}^{-1}$ at 510 and 1500 iterations, respectively, and the strengths at nontarget layer 4 were 0.0597 and $0.1087\ \text{cm}^{-1}$, respectively. In addition, the background noise fluctuation or standard deviation measured at nontarget layer 1 was increased with the iterations. The mean and the standard deviation at 510 iterations were 0.024 and $0.0041\ \text{cm}^{-1}$, whereas these values at 1500 iterations were 0.0267 and $0.0104\ \text{cm}^{-1}$.

As shown in Fig. 12(d), the reconstructed image improved a lot when the target depth was given. The maximum strength was $0.074\ \text{cm}^{-1}$, and its location was (0.5, −0.5). The −6-dB beam width was 2.63 cm, which was 12% better than that obtained from Fig. 12(a). The sidelobe was −6 dB from the peak, which was improved by 3 dB compared with Fig. 12(a).

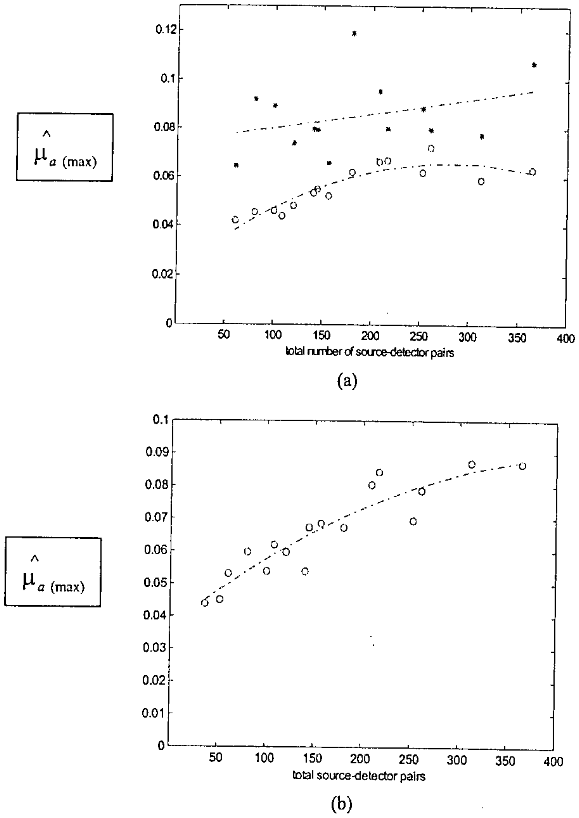

(a)

(b)

Fig. 13. Low-contrast target case. (a) Reconstructed $\hat{\mu}_{a(\max)}$ versus total source–detector pairs with the target depth available (stars) and the curve-fitting results (upper curve). Reconstructed $\hat{\mu}_{a(\max)}$ versus total source–detector pairs measured at target layer (circles) and the curve-fitting results (lower curve) and (b) at deeper nontarget layer 4.

C. Experimental Results of Reconstructed $\hat{\mu}_{a(\max)}$ versus Total Number of Source–Detector Pairs

With the iteration number normalized to the dense array case, we measured target strengths at target layer 3 and nontarget layer 4 for all sparse array configurations. Figure 13 shows the experimental data points (circles) of measured $\hat{\mu}_{a(\max)}$ versus the total number of source–detector pairs obtained at target layer 3 [Fig. 13(a)] and nontarget layer 4 [Fig. 13(b)]. The two curves were the fitting results of experimental points when we used second-order polynomials. In both layers, the $\hat{\mu}_{a(\max)}$ values were decreased when the total number of source–detector pairs was reduced. The reconstructed target strengths were reduced to less than 60% when the total pairs were less than 156 and 140 for target layer 3 and nontarget layer 4, respectively. The ultrasound-assisted reconstruction results are shown in Fig. 13(a) (stars), and the average reconstructed $\hat{\mu}_{a(\max)}$ for all array configurations was $0.085\ \text{cm}^{-1}$. Compared with the average of $0.055\ \text{cm}^{-1}$ obtained from optical imaging only at the target layer, a 30% improvement was achieved.

D. Experimental Results of Imaging Parameters versus Total Number of Source–Detector Pairs

The measured imaging parameters obtained from different array configurations are listed in Table 2. Similar to Table 1, listed are the measured parameters at target layer 3 and nontarget layer 4. The increase in beam width at the target layer was negligible for the arrays with more than 156 source-detector pairs and was more than 50% for the sparse arrays with total pairs less than this number. The sidelobes were progressively worse when the total

Table 2. Imaging Parameters Measured with Different Array Configurations: Lower-Contrast Target Case ($\mu_a = 0.10\ \text{cm}^{-1}$)

Parameter	Total Pairs														
	28 × 13	24 × 13	20 × 13	28 × 9	24 × 9	16 × 13	20 × 9	12 × 13	16 × 9	28 × 5	24 × 5	12 × 9	20 × 5	16 × 5	12 × 5
Target layer 3 (510 iterations)															
−6-dB beam width (cm)	1.83	1.98	2.02	2.24	1.86	2.09	2.42	*2.73*	*3.07*	*3.07*	*2.98*	*4.10*	*3.57*	*4.23*	*3.07*
Peak sidelobe (dB)	−6	−6	−7	−4	−3	−5	−2	−6	−3	−4	−3	−1	−3	−2	−2
$\hat{\mu}_{a(\max)}$ (cm^{-1})	0.06	0.06	0.07	0.06	0.07	0.07	0.06	0.05	0.06	0.05	0.05	0.04	0.05	0.05	0.04
$\lvert\hat{\mu}_{a(\max)} - (0,0)\rvert$ (cm)	0.5	0.5	0.7	1.0	0.7	0.7	0.7	0.7	0.7	1.11	1.11	1.11	1.0	1.0	1.58
Nontarget layer 4 (510 iterations)															
−6-dB beam width (cm)	3.36	3.42	3.31	4.81	3.08	3.28	4.69	4.20	5.49	5.57	5.15	4.88	6.62	8.49	8.81
Peak sidelobe (dB)	−8	−9	−8	−6	−7	−7	−5								
$\hat{\mu}_{a(\max)}$ (cm^{-1})	0.09	0.09	0.08	0.07	0.08	0.08	0.07	0.07	0.07	0.05	0.06	0.06	0.05	0.06	0.05
$\lvert\hat{\mu}_{a(\max)} - (0,0)\rvert$ (cm)	0.0	0.0	0.5	0.7	0.5	0.5	0.5	0.5	0.5	0.5	0.5	1.11	0.5	0.5	0.5
Nontarget layer 2 (510 iterations)															
$\hat{\mu}_{a(\max)}$ (cm^{-1})	0.062	0.058	0.054	0.048	0.051	0.049	0.047	0.046	0.047	0.054	0.064	0.034	0.060	0.064	0.049
$\lvert\hat{\mu}_{a(\max)} - (0,0)\rvert$ (cm)	0.70	0.70	0.70	0.5	0.70	1.12	0.5	1.12	0.0	0.70	0.0	0.50	0.0	0.0	0.70
Target layer only (56 iterations)															
−6-dB beam width (cm)	1.67	2.43	2.35	1.72	2.10	1.93	1.56	3.12	2.37	2.12	2.63	1.12	1.84	1.86	3.30
Peak sidelobe (dB)	−4	−5	−6	−3	−3	−6	−2	−6	−4	−4	−5	+5	−4	−3	−2
$\hat{\mu}_{a(\max)}$ (cm^{-1})	0.11	0.08	0.08	0.09	0.08	0.10	0.12	0.07	0.08	0.08	0.07	0.09	0.09	0.06	0.06
$\lvert\hat{\mu}_{a(\max)} - (0,0)\rvert$ (cm)	0.7	0.0	0.0	0.5	0.0	0.7	0.0	0.7	0.0	0.7	0.7	1.11	0.7	0.5	0.7

Note: Italicized entries are 50% broader than the dense array beam width.

pairs were reduced. At the target layer, the distance between the $\hat{\mu}_{a(\max)}$ location and the true target location was more than 1 cm for the arrays with total pairs less than 140. Table 2 then lists the measured peak image lobe at nontarget layer 2 and its location. The target appeared at nontarget layer 2 in all array configurations because of the lower SNR of the data. However, the target mass observed at this layer was much smaller than that at layers 3 and 4 in all cases. The last row in Table 2 shows the measured imaging parameters when the target depth was available to optical reconstruction. Compared with parameters obtained from optical imaging only, the −6-dB beam width was improved by 41% on average, and the reconstruction speed was approximately ten times faster; however, the sidelobe was 1 dB worse.

6. Discussion

In addition to the total number of source–detector pairs, the measured imaging parameters are also related to other system parameters, for example, modulation frequency and system noise. The 140-MHz modulation frequency chosen in this study is a typical frequency used by many research groups. Our system noise level, including both coherent and incoherent, is less than 10 mV peak to peak, which is sufficiently low. Therefore the results we obtained are pertinent to 3-D imaging using similar system parameters and reflection geometry.

In this study the target absorption coefficient was reconstructed from measurements. Similar studies can be done for the scattering coefficient as well. To reconstruct the scattering coefficient, we can use the scattering weight matrix derived by O'Leary[11] to relate the medium scattering variations with the measurements. Simultaneous reconstruction of both absorption and scattering coefficients in reflection geometry is also possible, provided that the absorption and scattering weight matrices are regulated carefully. Because the eigenvalues of the two matrices are significantly different, good regulation schemes are needed to balance the reconstructed absorption and scattering coefficients at each iteration. This subject is one of our topics for further study.

In this study the ultrasound-assisted optical reconstruction was demonstrated at a particular target layer. Similar studies can be done with multiple targets located at different layers. In the multiple target case, we can attribute measured perturbations to more layers instead of a single layer. However, the improvements in reconstructed optical properties and reconstruction speed may be less than that of the single-layer case.

Ultrasound has good imaging capability, and it can detect small lesions of a few millimeters in size. However, its specificity in cancer detection is not high as a result of overlapping characteristics of benign and malignant lesions. NIR imaging has high specificity in cancer detection; however, it suffers low resolution and lesion location uncertainty because of the diffused nature of the NIR light. The hybrid imaging that combines ultrasound imaging capability and NIR contrast has a great potential to overcome deficiencies of either method. As we reported in the paper, the target depth information can significantly improve the accuracy of the reconstructed optical absorption coefficient and reconstruction speed. In addition to use of *a priori* target depth information, the target spatial distribution provided by ultrasound can be used in optical reconstruction as well.[15] With the localized spatial and temporal target information, the accuracy of the reconstructed optical properties and the reconstruction speed can be improved further. To demonstrate this, we need an ultrasound imaging transducer located at the middle portion of the probe. We are currently pursuing this study.[23,24]

In this study the targets of different contrasts were located at the center position. We have also done studies with targets of different contrasts located at off-center positions. For an off-center target case, the effective number of source–detector pairs is less than that of the on-center target case because measurements from certain source–detector pairs do not contain much information about the target. For example, if a target is placed at ($x = 2, y = 2, z = 3.0$ cm), the measurements of source–detector pairs at the opposite corner of the probe contribute little to the image reconstruction. In one study, targets of high and low contrast were located at ($x = 2, y = 2, z = 3.0$ cm). The reconstructed maximum absorption coefficient at the target layer was related more to the total neighbor source–detector pairs. However, the maximum value at a deeper nontarget layer was related more to the total source–detector pairs and was decreased with the reduction of total pairs. Because the photons originated from distant sources and detected by distant detectors experience longer and more diffused scattering paths, they are likely to interact with the off-center target and contribute to the absorption estimate at the deeper layer. In the same study, the measured sidelobe levels were 4.5 and 2.0 dB poorer on average compared with the on-center high- and low-target cases, respectively. The beam widths were comparable to those measured from on-center cases.

7. Summary

The relationship between the total number of source-detector pairs and the imaging parameters of a reconstructed absorption coefficient was evaluated experimentally. A frequency-domain system of a 140-MHz modulation frequency was used in the experiments. Reconstruction at a selected target depth with *a priori* depth information provided by ultrasound was demonstrated. The results have shown that the reconstructed absorption coefficient and the spatial resolution of the absorption image were decreased when the total number of source-detector pairs was reduced. More than 160 source-detector pairs were needed to reconstruct the absorption coefficient within 60% of the true value and spatial resolution comparable to that obtained with the dense array. The contrast resolution was poorer in general because of edge artifacts and could be worse if significant larger iteration numbers are used for reconstruction. The error in target depth estimated from 3-D optical images was approximately 1 cm. With the *a priori* target depth information provided by ultrasound, the reconstruction can be done at a selected depth. Because the unknowns were reduced significantly, the reconstruction speed was approximately ten times faster than that without depth information. In addition, the accuracy of the reconstructed absorption coefficient was improved by 15% and 30% on average for high- and low-contrast cases, respectively. Furthermore, the measured −6-dB beam width was improved by 24% and 41% for high- and low-contrast cases, respectively. The sidelobe was 3 and 1 dB poorer for high- and low-contrast cases because the measurement noise was lumped to single-layer reconstruction instead of multiple layers.

In conclusion, ultrasound-assisted 3-D optical imaging has shown promising results to overcome the problems associated with the reconstruction by use of diffusive waves. With the target depth information provided by ultrasound, the reconstructed absorption coefficient was more accurate and the reconstruction speed was much faster.

We acknowledge the funding support of the Connecticut Innovation Program, the U.S. Department of Defense Army Breast Cancer Program (DAMD17-00-1-0217), the Windy Will Cancer Fund, Multidimensional Technology Inc., and the Research Foundation of the University of Connecticut.

References

1. S. Fantini, S. Walker, M. Franceschini, M. Kaschke, P. Schlag, and K. Moesta, "Assessment of the size, position, and optical properties of breast tumors *in vivo* by noninvasive optical methods," Appl. Opt. **37,** 1982–1989 (1998).
2. S. Zhou, Y. Chen, Q. Nioka, X. Li, L. Pfaff, C. M. Cowan, and B. Chance, "Portable dual-wavelength amplitude cancellation image system for the determination of human breast tumor," in *Optical Tomography and Spectroscopy of Tissue III*, B. Chance, R. Alfano, and B. Tromberg, eds., Proc. SPIE **3597,** 571–579 (1999).
3. R. M. Danen, Y. Wang, X. D. Li, W. S. Thayer, and A. G. Yodh, "Regional imager for low resolution functional imaging of the brain with diffusing near-infrared light," Photochem. Photobiol. **67,** 33–40 (1998).
4. T. McBride, B. W. Pogue, E. Gerety, S. Poplack, U. Osterberg, B. Pogue, and K. Paulsen, "Spectroscopic diffuse optical tomography for the quantitative assessment of hemoglobin concentration and oxygen saturation in breast tissue," Appl. Opt. **38,** 5480–5490 (1999).
5. M. A. Franceschini, K. T. Moesta, S. Fantini, G. Gaida, E. Gratton, H. Jess, M. Seeber, P. M. Schlag, and M. Kashke, "Frequency-domain techniques enhance optical mammography: initial clinical results," Proc. Natl. Acad. Sci. USA **94,** 6468–6473 (1997).
6. J. B. Fishkin, O. Coquoz, E. R. Anderson, M. Brenner, and B. J. Tromberg, "Frequency-domain photon migration measurements of normal and malignant tissue optical properties in human subject," Appl. Opt. **36,** 10–20 (1997).
7. T. L. Troy, D. L. Page, and E. M. Sevick-Muraca, "Optical properties of normal and diseased breast tissues: prognosis for optical mammography," J. Biomed. Opt. **1**(3), 342–355 (1996).
8. R. J. Grable, D. P. Rohler, and S. Kla, "Optical tomography breast imaging," in *Optical Tomography and Spectroscopy of Tissue: Theory, Instrumentation, Model, and Human Studies II*, B. Chance and R. Alfano, eds., Proc. SPIE **2979,** 197–210 (1997).
9. H. Jiang, K. Paulsen, U. Osterberg, B. Pogue, and M. Patterson, "Optical image reconstruction using frequency-domain data: simulations and experiments," J. Opt. Soc. Am. A **12,** 253–266 (1995).
10. W. Zhu, Y. Wang, Y. Deng, Y. Yao, and R. Barbour, "A wavelet-based multiresolution regularized least squares reconstruction approach for optical tomography," IEEE Trans. Med. Imaging **16**(2), 210–217 (1997).
11. M. A. O'Leary, "Imaging with diffuse photon density waves," Ph.D. dissertation (University of Pennsylvania, Philadelphia, Pa., 1996).
12. X. Li, T. Durduran, A. Yodh, B. Chance, and D. N. Pattanayak, "Diffraction tomography for biomedical imaging with diffuse-photon density waves," Opt. Lett. **22,** 573–575 (1997).
13. C. Matson and H. Liu, "Analysis of the forward problem with diffuse photon density waves in turbid media by use of a diffraction tomography model," J. Opt. Soc. Am. A **16,** 455–466 (1999).
14. C. Matson and H. Liu, "Backpropagation in turbid media," J. Opt. Soc. Am. A **16,** 1254–1265 (1999).
15. Q. Zhu, T. Dunrana, M. Holboke, V. Ntziachristos, and A. Yodh, "Imager that combines near-infrared diffusive light and ultrasound," Opt. Lett. **24,** 1050–1052 (1999).
16. Q. Zhu, D. Sullivan, B. Chance, and T. Dambro, "Combined ultrasound and near infrared diffusive light imaging," IEEE Trans. Ultrason. Ferroelectr. Freq. Control **46,** 665–678 (1999).
17. Q. Zhu, E. Conant, and B. Chance, "Optical imaging as an adjunct to sonograph in differentiating benign from malignant breast lesions," J. Biomed. Opt. **5**(2), 229–236 (2000).
18. M. Jholboke, B. J. Tromberg, X. Li, N. Shah, J. Fishkin, D. Kidney, J. Butler, B. Chance, and A. G. Yodh, "Three-dimentional diffuse optical mammography with ultrasound localization in human subject," J. Biomed. Opt. **5**(2), 237–247 (2000).
19. D. A. Boas, M. A. O'Leary, B. Chance, and A. G. Arjun, "Scattering of diffuse photon density waves by spherical inhomogeneities within turbid media: analytic solution and applications," Proc. Natl. Acad. Sci. USA **91,** 4887–4891 (1994).
20. W. Zhu, Y. Wang, and J. Zhang, "Total least-squares reconstruction with wavelets for optical tomography," J. Opt. Soc. Am. A **15,** 2639–2650 (1998).
21. P. C. Li, W. Flax, E. S. Ebbini, and M. O'Donnell, "Blocked element compensation in phased array imaging," IEEE Trans. Ultrason. Ferroelectr. Freq. Control **40,** 283–292 (1993).
22. G. H. Golub, "Some modified matrix eigenvalue problems," SIAM (Soc. Ind. Appl. Math.) Rev. **15,** 318–334 (1973).
23. D. Piao, X.-H. Ding, P. Guo, and Q. Zhu "Optimal distribution of near infrared sensors for simultaneous ultrasound and NIR imaging," in *Biomedical Topical Meetings*, Postconference Digest, Vol. 38 of OSA Trends in Optics and Photonics Series (Optical Society of America, Washington, D.C., 2000), pp. 472–474.
24. P. Guo, Q. Zhu, D. Piao, and J. Fikiet, "Combined ultrasound and NIR imager," in *Biomedical Topical Meetings*, Postconference Digest, Vol. 38 of OSA Trends in Optics and Photonics Series (Optical Society of America, Washington, D.C., 2000), pp. 97–99.

Simultaneous near infrared diffusive light and ultrasound imaging

Nan Guang Chen, Puyun Guo, Shikui Yan, Daqing Piao and Quing Zhu*

Electrical and Computer Engineering Department

University of Connecticut, Storrs, CT 06269

Abstract

We have constructed a near real-time combined imager suitable for simultaneous ultrasound and near infrared (NIR) diffusive light imaging and co-registration. The imager consists of a combined hand-held probe and the associated electronics for data acquisition. A two-dimensional ultrasound array is deployed at the center of the combined probe and 12 dual wavelength laser source fibers (780 nm and 830 nm) and 8 optical detector fibers are deployed at the periphery. We have experimentally evaluated the effects of missing optical sources in the middle of the combined probe upon the accuracy of the reconstructed optical absorption coefficient, and assessed the improvements of reconstructed absorption coefficient with the guidance of the co-registered ultrasound. The results have shown that when the central ultrasound array area is in the neighborhood of 2×2 cm^2, which corresponds to the size of most commercial ultrasound transducers, the optical imaging is not affected. The results have also shown that the iterative inversion algorithm converges very fast with the guidance of *a priori* three-dimensional target distribution, and only one iteration is needed to reconstruct accurate optical absorption coefficient.

OCIS codes: 170.0170, 170.3010, 170.5270, 170.7170, 170.3830

---

* Correspondence: Quing Zhu, Electrical and Computer Engineering Department, University of Connecticut, Storrs, CT 06269 (Tel:860-486-1815, e-mail zhu@engr.uconn.edu)

1. Introduction

Ultrasound is used extensively for differentiation of cysts from solid lesions in breast examinations and it is routinely used in conjunction with mammography. Ultrasound can detect breast lesions a few mm in size.[1] However, its specificity in breast cancer detection is not high as a result of overlapping characteristics of benign and malignant lesions.[2-3] Optical imaging based on diffusive near- infrared (NIR) light has the great potential to differentiate tumors from normal breast tissues through determination of tissue parameters, such as blood volume, blood O_2 saturation, tissue light scattering, water concentration, and the concentration and lifetime of exogenous contrast agents.[4-12] As a potential diagnostic tool, however, NIR diffusive light imaging suffers from low spatial resolution and lesion location uncertainties due to intense light scattering in tissue.

Most NIR imaging reconstruction algorithms are based on tomographic inversion techniques.[13-19] Reconstruction of tissue optical properties in general is underdetermined and ill-posed because the total number of unknown optical properties always exceeds the number of measurements and the perturbations produced by the heterogeneities are much smaller than the background signals. In addition, the inversion reconstruction algorithms are very sensitive to measurement noise and model errors.

Our group and others have introduced a novel hybrid imaging method that combines the complementary features of ultrasound and near-infrared diffusive light imaging.[20-24] The hybrid imaging obtains co-registered ultrasound and NIR diffusive light images through simultaneous deployment of an ultrasound array and NIR source detector fibers on the same probe.[20,21,23] Co-registration permits joint evaluation of acoustic and optical properties of breast lesions, and enables the use of lesion morphology provided by high-resolution ultrasound to improve the lesion optical property estimate. With the *a priori* knowledge of lesion location and shape provided by co-registered ultrasound, NIR imaging reconstruction can be localized within specified 3-D regions. As a result, the reconstruction is over-determined because the total number of unknown optical properties is reduced significantly. In addition, the reconstruction is less sensitive to noise because the convergence can be achieved with a small number of iterations.

The clinical use of the combined diagnosis relies on the co-registration of both ultrasound and NIR sensors at the probe level. Conventional ultrasound pulse echo imaging requires an imaging transducer be located on top of the target, while NIR diffusive light imaging is feasible when the optical source and detector fibers are distributed at the periphery of the ultrasound transducer. However, the effects of missing optical sources in the middle of the combined probe upon the accuracy of the reconstructed optical properties have to be evaluated. In addition, the improvements of reconstructed optical properties with the guidance of the co-registered ultrasound need to be quantitatively assessed. Furthermore, real-time data acquisition is necessary to avoid errors in co-registration caused by patient motion during the clinical experiments. In this paper, we report our experimental results on optimal probe configuration and we quantify the improvements on reconstructed optical properties using a combined probe. We also demonstrate simultaneous combined imaging with a near real-time imager.

2. NIR diffusive wave imaging

We have used Born approximation to relate the scattered field $U'_{sc}(\mathrm{r},\omega)$ measured at the probe surface to absorption variations in each volume element within the sample. In the Born approximation, the scattered wave originated from a source at r_{si} and measured at r_{di} can be related to the medium absorption heterogeneity $\Delta\mu_a(\mathrm{r}_{vj})$ at r_{vj} by

$$[U_{sd}]_{MX1} = [W]_{MXN}\{\Delta\mu_a\}_{NX1} \qquad (1)$$

where M is the total number of source-detector pairs, N is the total number of imaging voxels, and $W_{ij} = G(\mathrm{r}_{vj},\mathrm{r}_{di},\omega)U_{inc}(\mathrm{r}_{vj},\mathrm{r}_{si},\omega)v\Delta\mathrm{r}_v^{\,3}/\overline{D}$ is the weight matrix given in Ref. 18. $G(\mathrm{r}_{vj},\mathrm{r}_{id},\omega)$ and $U_{inc}(\mathrm{r}_{vj},\mathrm{r}_{si},\omega)$ are Green function and incident wave, respectively. ω is the modulation frequency and $\overline{D}$ is the average or background diffusion coefficient, which is the average value over the background or whole tissue.

With M measurements obtained from all possible source-detector pairs in the planar array, we can solve N unknowns of μ_a by inverting the above matrix equation. In general, the perturbation Eq. (1) is underdetermined (M<N) and ill-posed.

NIR imaging by itself generally has poor depth discrimination. However, ultrasound is excellent in providing accurate target depth. Once the target depth is available from co-registered ultrasound, we can set $\Delta\mu_a$ of non-target depth equal to zero. This implies that all the measured perturbations originate from the particular depth that contains the target. Since the number of unknowns is reduced significantly, the reconstruction converges very fast. In Ref [23], we have reported that with *a priori* target depth provided by ultrasound, the accuracy of the reconstructed μ_a has been improved by 15%-30% on average and the speed of reconstruction has been improved by an order of magnitude. In this paper, we furthermore demonstrate that with the three-dimensional target distribution provided by co-registered ultrasound, the accuracy of reconstructed μ_a and the reconstruction speed can be further improved.

To solve the unknown optical properties of Eq. (1), we have used the total least-squares (TLS) method [25-26] to iteratively invert the equation. The TLS performs better than other least-square methods when the measurement data are subject to noise and the linear operator W contains errors. We have found that the TLS method provides more accurate reconstructed optical properties than other least square methods and we have adopted TLS in solving inverse problems. It has been shown in Ref. [27] that the TLS minimization is equivalent to the following minimization problem.

$$\min \frac{\|U_{sd} - WX\|^2}{\|X\|^2 + 1} \qquad (2)$$

where X represents unknown optical properties. The conjugate gradient technique has been employed to iteratively solve Eq. (2).

3. Methods

A. Combined probe and imaging geometry

There are four basic requirements to guide the design of the combined probe. First, reflection geometry is preferred because conventional ultrasound scan is performed with this geometry. Second, ultrasound array needs to occupy the center of the combined probe for coherent imaging. Third, NIR sources and detectors have to be distributed at the periphery. Since photon propagation distribution exhibits a "banana" shape, imaging of the tissue volume underneath the probe is feasible even through there are no sources and detectors deployed in the central portion of the probe. Fourth, the minimum source-detector separation should be larger than 1 cm for diffusion approximation to be valid, and the maximum separation should be ~ 8-9 cm for effectively probing depths of 3-4 cm.

Based on these requirements we have deployed 12 dual-wavelength optical source fibers and 8 detector fibers over a 9×9 cm^2 probe area (see Figure 1). The minimum and maximum source-detector separations in the configuration are 1.4 cm and 8 cm, respectively. To study the effect of the central "optical hole" upon the accuracy of the reconstructed optical properties, we have compared the reconstruction results with an extra center source and without the center source. The configuration without the center source corresponds to a 2×2 cm^2 hole area. We further moved the non-center 12 sources and 8 detectors toward periphery by leaving a 3×3 cm^2 hole area in the middle. Figure 2 shows the picture of a combined probe with the 3×3 cm^2 central area occupied by an ultrasound array. The ultrasound array consists of 64 elements made of 1.5 mm diameter piezoelectric (PZT) transducers (Valpey Fisher Inc). The transducers are deployed in a rectangular matrix with 4 mm spacing in both x and y directions. The center frequency of the transducer is 6 MHz and the bandwidth is 40%. The transducers are made from the same piece of PZT material. Therefore, the gain difference among different transducers is less than 3 dB. 12 dual-wavelength optical laser diode sources (760 nm and 830 nm) and 8 Photo Multiplier (PMT) detectors are coupled to the probe through optical fibers, which are deployed at the periphery of the 2-D ultrasound array. This hybrid array deployment compromises ultrasound coherent imaging and NIR diffusive light imaging characteristics.

The $9\times9\times4$ cm^3 image volume underneath the probe is discretized into voxels of size $0.4\times0.4\times1$ cm^3. There is a trade-off between the accurate estimation of the weight matrix W and the voxel size. Since W_{ij} is a discrete approximation of the integral $\int_v G(\mathrm{r}_v,\mathrm{r}_{d,}\omega)U_{inc}(\mathrm{r}_v,\mathrm{r}_s,\omega)\frac{v}{D}d\mathrm{r}_v^3$, it is more accurate when the voxel size is smaller. However, the total number of reconstructed unknowns will increase dramatically with the decreasing voxel size. Furthermore, the rank of W does not increase in the same order as the total number of voxels when the voxel size decreases. This suggests that neighboring W_{ij}s are correlated when the voxel size is smaller and further decrease in voxel size will not add more independent information to the weight matrix. We have found that $0.4\times0.4\times1$ cm^3 voxel size is a good compromise. Therefore, we have used this voxel size in image reconstructions reported in this paper.

B. Experimental Systems

NIR imaging system

We have constructed a NIR frequency domain imaging system. The block diagram of the system is shown in Figure 3. This system has 12 dual-wavelength source channels and 8 parallel receiving channels. On the transmission part, 12 pairs of dual wavelength (780nm and 830nm) laser diodes are used as light sources, and their outputs are amplitude modulated at 140.000 MHz. Each one of the 12 optical combiners (OZ Optics Inc.) looks like a Y adapter, guiding the emission of two diodes of different wavelengths through the same thin optical fiber (about 0.2 mm in diameter). To reduce noise and interference, an individual driving circuit is built for each diode. As a laser diode works in series, a control board that interprets instructions from a PC is used to coordinate operations of associated components. When a single transmission channel is selected, it turns on corresponding driving circuit so that a DC driving current can be set up for the diode. At the same time, a selected signal is sent to a RF switching unit, which distributes a RF signal to the right channel to modulate the optical output. On the reception part, 8 Photo Multiplier Tubes (PMTs) are employed to detect diffusely reflected light from turbid media. Each PMT is housed in a sealed aluminum box, shielding both environment lights and electromagnetic fields, while an optical fiber (3 mm in diameter) couples NIR light from the detection point to the reception window of the PMT. The electrical signal converted from the optical input is generally very weak and rather high in frequency, so high gain amplification and frequency transform are necessary before it can be sampled by an A/D board inside the PC. We have built 8 parallel heterodyne amplification channels in order to measure the response of all detectors simultaneously, to thus reduce the data acquisition time. Each amplification channel consists of a RF amplifier (40dB), a mixer where RF signal (OSC1, 140.000 MHz) is mixed with a local oscillator (OSC2, 140.020 MHz) and, a band pass filter centered at 20 KHz, and a low frequency amplifier of 30dB. The heterodyned two-stage amplification scheme helps suppress wide band noises efficiently. A reference signal of 20 KHz is also generated by directly mixing OSC1 and OSC2, which is necessary for retrieving phase shifts. Eight detection signals and one reference are sampled, converted, and acquired into the PC simultaneously, in which the Hilbert transform is used to compute the amplitude and phase of each channel. The entire data acquisition takes less than one minute, which is fast enough to acquire data from patients.

One of the challenges encountered in designing a NIR imaging system is the huge dynamic range of signals received at various source-detector distances. For example, for a semi-infinite phantom made of 0.5% Intralipid solution, the amplitude measured at 1 cm away from a source is about 5000 times larger than that at 8 cm separation. In addition, the perturbation due to an embedded heterogeneity with optical properties similar to a tumor is normally a few percent of the background signal. As a result, a reflection mode NIR imaging system should have at least 120 dB dynamic range to probe a target up to 4 cm in depth. It's very hard to build amplifiers working linearly over such a wide dynamic range. We overcome this difficulty by implementing two-level source outputs. The DC output of a laser diode is controlled by adjusting its feedback loop, while the RF signal is switched simultaneously via a two-step attenuator (no attenuation or 30 dB attenuation). When the source and detector are close to each other, the source is controlled to yield low-level output. When the separation gets larger, 30 dB higher output level should be used. With this two-level source scheme, our system achieved fairly good linearity over a wide range of source-detector separations (from 1.5 to 8 cm).

Since parameters of individual laser diode and/or PMT vary considerably from one to another, we have to calibrate the gain and phase shift for each channel. A set of measurements obtained from all source-detector pairs placed on the boundary of a homogeneous medium are

$$\overline{A}_{\alpha\beta} \text{ and } \overline{\phi}_{\alpha\beta}, \qquad \alpha = 1,2,\ldots,m; \;\; \beta = 1,2,\ldots,n.$$

Here, amplitude $\overline{A}_{\alpha\beta}$ and phase $\overline{\phi}_{\alpha\beta}$ are related to source α and detector β, while m and n are the total number of sources and detectors respectively. From the diffusion theory, we can obtain the following set of equations,[7]

$$\begin{cases} \overline{A}_{\alpha\beta} = I_s(\alpha) I_d(\beta) \dfrac{\exp(-k_i \rho_{\alpha\beta})}{\rho_{\alpha\beta}^2} \\ \overline{\phi}_{\alpha\beta} = \varphi_s(\alpha) + \varphi_d(\beta) + k_r \rho_{\alpha\beta} \end{cases}$$

in which $I_s(\alpha)$ and $\varphi_s(\alpha)$ are relative gain and phase delay associated with source channel α, $I_d(\beta)$ and $\varphi_d(\beta)$ are similar quantities associated with detector channel β. $\rho_{\alpha\beta}$ is the corresponding separation, and $k_r + jk_i$ is the complex wave number. We obtain the following set of linear equations by taking logarithm of the above equations related to amplitude

$$\begin{cases} \log(\rho_{\alpha\beta}^2 \overline{A}_{\alpha\beta}) = \log(I_s(\alpha)) + \log(I_d(\beta)) - k_i \rho_{\alpha\beta} \\ \overline{\phi}_{\alpha\beta} = \varphi_s(\alpha) + \varphi_d(\beta) + k_r \rho_{\alpha\beta} \end{cases} . \tag{3}$$

Although the optical properties of the calibration medium are known in advance, we leave the wave number as unknown. (The main reason that we leave k_r and k_i as unknowns is that we want to include this calibration method in our clinical experiment procedures. That means *in vivo* calibration with the probe on a human breast. In this case, the optical properties of the background medium are completely unknown. We have verified our calibration method by comparing the best fitted k 's with real values. The results of using 0.5~0.8% Intralipid solutions always gave scattering and absorption coefficients with a rather good accuracy.) With the two unknown wave numbers included, the total number of unknowns is $2(m+n+2)$, which is generally far smaller than the number of measurements $m \times n$. Consequently, Eq. (3) is over-determined. We can solve all $I_s(\alpha), I_d(\beta), \varphi_s(\alpha)$ and $\varphi_d(\beta)$ terms as well as two unknown wave numbers in a least square sense. Then all measurements can be calibrated accordingly. The results of amplitude $A_{\alpha\beta} = \dfrac{\exp(-k_i \rho_{\alpha\beta})}{\rho_{\alpha\beta}^2}$ and phase $\phi_{\alpha\beta} = k_r \rho_{\alpha\beta}$ after calibration are shown in Figure 4. As one can see, the calibrated amplitude (log $\rho_{\alpha\beta}^2 A_{\alpha\beta}$) and phase from various source-detector pairs change linearly with distance.

Ultrasound system

The ultrasound system diagram is shown in Figure 5, and the system consists of 64 parallel transmission and receiving channels. Each transmission circuit can generate a high voltage pulse of 200 ns duration (6 MHz) with 125 volts peak to peak to the connected transducer. Each receiving circuit has two-stage amplifiers followed by an A/D converter with 40 MHz sampling frequency. The amplifier gain can be controlled based on the target strength. A group of transmission channels can be addressed simultaneously to transmit pulses from neighbor transducers with specified delays and, therefore, to focus the transmission beam. The retuned signals can be simultaneously received by a group of transducers and the signals can be summed with specified delays to form a receiving beam.

The data acquisition procedure is the following. The first 9-element neighbor subarray (dashed rectangle in Figure 6) from the 64-element transducer array and the corresponding channels are chosen, and then the transmission delay profiles are generated in the computer according to the pre-specified focal depth. The delay profile data are transferred to the 64-channel delay profile generator, which triggers the 64 high voltage pulsers as well as the receiving channels. The returned ultrasound signals are amplified by two stage amplifiers and sampled by A/D converters. The data are buffered in the memories and are read by the computer after the entire data acquisition is completed. The second subarray (solid rectangle on Figure 6) is chosen and the same data acquisition process is repeated. A total of 64 subarrays is used in the data acquisition. After the 64-subarray data acquisition is completed, the data stored in the memories are read by the computer for image formation. The entire data acquisition and imaging display are done in about 5 seconds, which is fast enough for clinical experiments. To ensure good SNR, all the electronics are done using printed circuit boards.

Figure 7 shows the picture of the entire system and the combined probe. Both NIR system (top) and ultrasound system (bottom) are mounted on a hospital cart. The combined probe, which houses the ultrasound array and the NIR source detector fibers, is designed to be hand held to scan patients.

C. Phantoms

0.5-0.6% Intralipid solutions are used to mimic normal human breast tissues in all experiments and the corresponding reduced scattering coefficient $\mu_s^{'}$ ranges from 5 cm^{-1} to 6 cm^{-1}. The Intralipid is contained in a large fish tank to set up approximately a semi-infinite homogeneous phantom. Small semi-spherical balls (1 cm in diameter), made of acrylamide gel [21], are inserted into Intralipid to emulate lesions embedded in a breast. The reduced scattering coefficients of the gel phantoms are similar to that of the background medium ($\mu_s^{'} \approx 6$ cm^{-1}), and the absorption coefficients are changed to different values by adding different concentrations of India ink to emulate high contrast ($\mu_a = 0.25 \, cm^{-1}$) and low contrast ($\mu_a = 0.1 \, cm^{-1}$) lesions. Ultrasound scattering particles of 200 µm in diameter are added to the gel phantom before the gel has been formed.

4. Experimental Results

A. Effects of missing optical sources in the combined probe

A series of experiments was conducted to estimate the optimal hole size. Three probe configurations were investigated, which were (a) no-hole, (b) 2 × 2 cm^2 central hole, and (c) 3 $\times 3$ cm^2 hole probes. The no-hole probe was essentially the same as case (b) except that an additional light source was added in the middle. Figure 8 shows reconstructed NIR images for on-center targets of high (μ_a = 0.25 cm^{-1}, left column) and low contrast (μ_a =0.1 cm^{-1}, right column) located 2.5 cm deep inside the Intralipid. The fitted background μ_a and μ_s' are 0.015 cm^{-1} and 5.36 cm^{-1}, respectively. With the target depth provided by ultrasound, we performed reconstruction in the target layer. The centers of the voxels in this layer were (x, y, 2.5 cm), where x and y were discrete spatial x-y coordinates, and the thickness of the layer was 1 cm. For the high contrast target case, there are no important differences in image quality associated with different probes (Figure 8(a), (c)) except that with a 3 cm by 3 cm hole. The first row of Table 1 provides measured maximum μ_a values from the corresponding images. Because of the low spatial resolution of diffusive imaging, the boundaries of targets are not well defined. The maximum value is a better estimation of reconstructed target μ_a. From no-hole to 2×2 cm^2, the reconstructed maximum μ_a decreases slowly. But for 3×3 cm^2, the maximum μ_a drops suddenly to 0.104 cm^{-1}, which is less than half of the original value. Another imaging parameter we measured is the full width at half maximum (FWHM) of the corresponding images. Since the image lobes were elliptical in general, we measured the widths of longer and shorter axes and used the geometric mean to estimate FWHM. The results are shown in the second row of the Table 1, and the FWHM almost increases with the hole size. We also measured image artifact level, which was defined as the ratio of the peak artifact to the maximum strength of the image lobe and was given in decibels. The results are shown in the third row. No artifacts were observed in the images of no-hole and 2×2 cm^2 hole probes. However, the peak artifact level at the -14.3 dB level was measured in the image of the 3×3 cm^2 hole probe. When the contrast was low, the reconstructed maximum absorption coefficients and measured FWHMs were essentially the same for the no-hole and 2×2 cm^2 hole probes. However, the reconstructed maximum value dropped to 60% of the true value for the 3×3 cm^2 probe. The artifact levels measured in images of three probe configurations were similar and were worse than the high contrast case. The image artifacts are related to the reconstruction algorithm. When the target contrast is weak and/or the SNR is low, the inversion algorithm produces artifacts around the edges of the images.

For shallow targets (here we set the target depth to be 1.5 cm) the NIR system has relatively poorer performance. This is due to less source-detector pairs experiencing the existence of a shallow absorber. As shown in Figure 9, image artifacts are obviously worse compared with Figure 8. However, the conclusion about the hole size of the probe remains true. Table 2 lists all the measured imaging parameters obtained from three probe configurations. While a 3×3 cm^2 hole is somewhat too big to get good enough results, the optimal hole size is in the neighborhood of 2×2 cm^2. This optimal size is about the size of commercial ultrasound transducers.

In the above studies, we have used the iteration number obtained from the no-hole configuration for the rest of the configurations. Ideally, the iteration should stop when the object function (see Eq. (2)) or the error performance surface reaches the noise floor. However, system noise, particularly coherent noise, was difficult to estimate from experimental data. In general, we have found that the reconstructed values were closer to true values when the object function reached about 5% to15% of the initial value (total energy in the measurements). Therefore, we have used this criterion (~10% of the initial value) for the no-hole configuration. Since the SNR of the date decreased with the increase in hole-size, we could not find consistent criterion for both no-hole and hole data. Therefore, we have used the same iteration number obtained from the no-hole case for the hole configurations and the comparison was based on the same iteration number.

B. Ultrasound-guided NIR imaging

Three-dimesional ultrasound images can provide 3-D distributions of targets. With the *a priori* target depth information, the optical reconstruction can be improved significantly. An example is given in Figure 10. The target again was 1 cm diameter gel ball of low ($\mu_a = 0.1$ cm^{-1}) optical contrast and was embeded at approximately (0, 0, 2.5 cm) inside the Intralipid medium. The fitted background μ_a and μ_s' are 0.02 cm^{-1} and 5.08 cm^{-1}, respectively. The combined probe shown in Figure 2 was used to obtain the ultrasound and NIR data simultaneously. Figure 10 (a) shows an A-scan line of a returned ultrasound echo signal received by one ultrasound transducer located on top of the target. As acoustic scatters were uniformly distributed in the target, signals were reflected from inside the target as well as from the surfaces. The reflected signals from the front and back surfaces of the gel ball can be clearly identified in the echo signal. Based on the target depth, we reconstructed the optical absorption coefficient at the target depth only (1 cm in thickness) by setting the purturbations from the other depths equal to zero. We also performed 3-D optical only reconstruction. Figure 10 (b) shows the recontructed absorption image from a 3-D optical only reconstruction (layer three of voxel coordinates (x,y, 2.5cm) and 1 cm thicknss), while Figure 10 (c) shows the reconstructed image of the corresponding target from ultrasound guided reconstruction. For optical only reconstruction, the algorithm did not converge to a localized spatial region and the image contrast was poor. The measured maximum absorption coefficient was 0.088 cm^{-1}, which was close to the true value. However, the measured spatial location of the maximum value was (-1.6 , -1.2 cm) which was too far from the true target location. With the *a priori* target depth, the reconstruction performed at the target layer can localize the target to the correct spatial position. The measured maximum absorption coefficient was 0.12 cm^{-1} and its location was (0, 0.4 cm) which was very close to the true target location. This example demonstrates that *a priori* target depth can significantly improve the reconstruction accuracy and target localization.

In addition to the use of *a priori target* depth information, we can also use target spatial distribution provided by ultrasound to guide the reconstruction. We performed a set of experiments with two targets located at 2.5 cm depth inside the Intralipid. Each target is a 1 cm^3 gel cube containing ultrasound scatters. For optical properties, they both could be high contrast ($\mu_a = 0.25 cm^{-1}$) or low contrast ($\mu_a = 0.1 cm^{-1}$), but had the same reduced scattering coeficient as the background. The fitted background μ_a and $\mu_s^{'}$ are 0.017 cm^{-1} and 4.90 cm^{-1}, respectively. One target was appproximately centered at (-1.0, -1.0, 2.5 cm), while the other was at (1.0, 1.0, 2.5 cm). The distance between the centers of the two targets was 2.8 cm.

Figure 11(a) is the ultrasound image of two high contrast targets. As the field of view of the ultrasound system was nearly a 3 cm by 3 cm square, these two targets appeared at diagonal corners. The measured peak positions of the two targets were (-0.6, -1.0 cm) and (1.0, 1.0 cm), which differed from the true target locations by only one voxel. The low contrast of the ultrasound image is related to the speckle noise. Since our ultrasound array is sparse, the imaging quality is not state-of-the-art (see more discussion in Section 5). The NIR image of these targets was obtained simultaneously and is shown in Figure 11(b). The reconstruction was performed at the target layer by taking advantage of target depth information. A total of 123 iterations was used to obtain Figure 11 (b). The measured peak positions of the two targets were (-1.4, -1.0 cm) and (0.6, 0.6 cm), which were one voxel off from the true target locations (-1.0,

-1.0 cm) and (1.0, 1.0 cm), respectively. The corresponding reconstructed absorption coefficients were 0.242 cm^{-1} and 0.251 cm^{-1}, which were close to true values. However, the two targets were almost connected to each other and their spatial localization was poor. For low contrast targets, the ultrasound image is shown in Figure 11 (c) and the measured peak locations of the two targets were (-1.0, -0.6 cm) and (0.6, 1.0 cm), which differed from true target locations by only one voxel. The corresponding NIR image is shown in Figure 11 (d) and the measured peak locations of the two targets were (-2.2, -1.0 cm) and (0.6, 1.0 cm). The left target was off the true location by three voxels. The corresponding reconstructed absorption coefficients were 0.063 cm^{-1} and 0.1004 cm^{-1} at 87 iteration steps. As one can see, the target shape and localization were poorer than those in the high contrast case. In addition, an artifact appeared at the edge of the image.

From the co-registered ultrasound images, we obtained spatial distributions of the two targets and specified target regions. Figure 12 (a) and (c) show the –6 dB contour plots of Figure 11 (a) and (c). Applying the same reconstruction scheme to these specific regions, we obtained Figure 12 (b) and (c) in 1 iteration. The reconstructed absorption coefficients were 0.2357 cm^{-1} and 0.219 cm^{-1} for the two high contrast target cases, and 0.123 cm^{-1} and 0.131 cm^{-1} for the low contrast case. We can see much better improvement in the low contrast target case, when comparing Figure 12 (d) with Figure 11 (d). This example has demonstrated that target morphology information provided by ultrasound can be used to guide the optical reconstruction in the specified regions.

The result regarding the iteration step is significant. As we discussed earlier, there is no known stopping criterion to terminate the iteration because it is very difficult to estimate the noise level in the measurements. With the *a priori* target depth and spatial distribution provided by co-registered ultrasound, we can obtain an accurate optical absorption coefficient in one iteration. Therefore, no stopping criterion is needed for the inversion algorithms. However, this result will need to be further evaluated with more samples of different contrasts.

5. Discussion

Commercial ultrasound scanners use 1-D probes which provide 2-D images of x-z views of the targets, where x and z are spatial and propagation dimensions, respectively. Such x-z images cannot co-register with NIR images, which are obtained from x-y views of the targets. Our current 2-D ultrasound array is capable of providing x-y views of the targets, which can be used to co-register with NIR images. However, the array is sparse and, therefore, the image resolution is not state-of-the-art. Nevertheless, its spatial resolution is comparable to NIR imaging and can be used to guide NIR image reconstruction. With 3-D ultrasound guidance, only one iteration is needed to obtain accurate absorption coefficients. This result is significant because no stopping criterion is necessary. More studies with a variety of target contrasts and locations will be performed to verify this result.

We have purchased a 2-D state-of-the-art ultrasound array of 1280 transducer elements and we are building a multiplexing unit for our 64-channel electronics. In addition, the new 2-D transducer size is about $2 \times 3\ \text{cm}^2$, which is in the neighborhood of the optimal hole size we have found through this study. With the new 2-D ultrasound transducer, we will be able to obtain high-resolution ultrasound images and delineate the target boundaries with finer details for optical reconstruction.

Ultrasound contrast depends on lesion acoustic properties and NIR optical contrast is related to lesion optical properties. Both contrasts exist in tumors but the sensitivities of these two modalities may be different. It is possible that some early stage cancers have NIR contrast but are not detectable by ultrasound. It is also possible that some lesions have acoustic contrast but no NIR contrast or low NIR contrast. However, ultrasound is routinely used as an adjunct tool to X-ray mammography, and the detection sensitivity of ultrasound together with palpation and X-ray mammography is 98.4% according to a clinical trial reported in Ref [1]. For those lesions that are seen in X-ray and ultrasound images, we will be able to use ultrasound guidance as reported in this paper to quantify the light absorption as well as other optical parameters more accurately. The role of optical imaging is to add more specificity to the ultrasonically detected lesions. For those lesions that are seen by X-ray and not shown well in ultrasound, we will need to carefully mark the corresponding lesion regions in ultrasound images and reconstruct NIR images of these regions as well. Optical imaging will again add more specificity to the conventional imaging method. Since X-ray provides projection slices with no depth information, direct X-ray guidance to optical imaging may not yield meaningful results. It would be desirable if we could obtain sensitivity of optical imaging alone. However, light scattering is a main problem that prevents the accurate and reliable localization of lesions.

In the reported phantom studies, we assigned zero perturbations to the regions where no targets were present. In clinical studies, we plan to segment the ultrasound images and specify different tissue types as well as suspicious regions in the segmented images. We then reduce the reconstructed optical unknowns by assigning unknown optical properties to different tissue types as well as to suspicious regions. Finally, we reconstruct the reduced sets of unknown optical properties. We expect more accurate estimation of reconstructed optical properties and fast convergence speed, as reported in the paper. However, it is still too early to judge the clinical performance of the combined method; further clinical studies are needed.

Probing regions of the banana-shaped diffusive photons depend on source-detector separations and measurement geometry. For a semi-infinite geometry, the probing regions extend further into the medium when source-detector separation increases. This is why we have multiple source-detector pairs of various separations to detect targets at variable depths from 0.5 cm to 4 cm. Of course, it is hard to achieve uniformity sensitivity in the entire region of interest. For example, a superficial target (~1cm deep) would cause very strong perturbations when it is close to a source or a detector, but will result in much weaker signals when it is located deeper. Normalization of scattering photon density waves with respect to the incident waves makes it possible for reconstruction algorithms to handle the huge dynamic range of signals and to detect a target as deep as 4 cm. This normalization procedure was applied to the reconstruction algorithm used to obtain the reported images.

In this study, the target absorption coefficient was reconstructed from the measurements. Since the target μ_s' was similar to the background μ_s', the coupling between μ_a and μ_s' in our measurements was negligible. We also did experiments with gel phantom made with Intralipid of the similar concentration to the background and did not observe perturbation beyond the noise level. Similar reconstruction studies can be done for scattering coefficients as well. Simultaneous reconstruction of both absorption and scattering coefficients is also possible. Since the eigenvalues of the absorption and scattering weight matrixes are significantly different, good regulation schemes are needed for simultaneous reconstruction. This subject is one of our topics for further study.

5. Summary

We have constructed a near real time imager that can provide co-registered ultrasound and NIR images simultaneously. This new technique is designed for improving the specificity of breast cancer diagnosis. Since the ultrasound transducer needs to occupy the central region of the combined probe, a series of experiments has been conducted to investigate the effects of missing optical sensors in the middle of the combined probe upon the NIR image quality. Our results have shown that as long as the central ultrasound transducer area is in the neighborhood of 2×2 cm^2, essentially similar reconstruction results as those of no missing optical sensors in the middle of the combined probe can be obtained. This 2×2 cm^2 dimension is about the size of most commercial ultrasound phased-array transducers. When the central missing optical sensor area is increased to 3×3 cm^2, however, the reconstructed values are obviously lower than real values. If we increase the iteration steps, artifacts in the reconstructed images would soon become dominant.

With the target 3-D distribution provided by co-registered ultrasound, significant improvements in algorithm convergence and reconstruction speed have been achieved. In general, *a priori* target depth information guides the inversion algorithm to reconstruct the heterogeneities at the correct spatial locations and improves the reconstruction speed by an order of magnitude. In addition, *a priori* target spatial distribution can further reduce the iteration to one step and also obtain accurate optical absorption coefficients. Given the fact that no known stopping criterion is available, this result is significant because no iteration is needed. However, this result will need to be evaluated with more samples of different contrasts.

6. Acknowledgements

We would like to thank the following for their funding support: the State of Connecticut, DOD ARMY Breast Cancer Program (DAMD17-00-1-0217, DAMD17-01-1-0216), the Research Foundation of the University of Connecticut, and Multiple-Dimensional Technology, Inc.

References

1. T. A, Stavros, D. Thickman, C. Rapp, "Solid breast nodules: use of sonography to distinguish between benign and malignant lesions," Radiology **196**, 123-134 (1995).
2. E. A. Sickles, R.A. Filly, P. W. Callen, "Benign breast lesions: ultrasound detection and diagnosis," Radiology **151**, 467-470 (1984).
3. V. P. Jackson , "The role of US in breast imaging," Radiology **177**, 305-311 (1990).
4. B. Tromberg, N. shah, R. Lanning, A. Cerussi, J. Espinoza, T. Pham, L. Svaasand and J. Butler, "Non-Invasive in vivo characterization of breast tumors using photon migration spectroscopy," Neoplasia **2**, 26-40 (2000).
5. S. Fantini, S. Walker, M. Franceschini, M. Kaschke, P. Schlag, K. Moesta, "Assessment of the size, position, and optical properties of breast tumors in vivo by noninvasive optical methods," Appl. Opt. **37**, 1982-1989 (1998).
6. S. Nioka , Y. Yung, M. Schnall, S. Zhao, S. Orel, C. Xie , B. Chance, "Optical imaging of breast tumor by means of continuous waves," Oxygen Transport to Tissue XVII (Neoto EM ed) Plenum Press Corp., New York (1992).

7. R.M. Danen, Yong Wang, X.D. Li, W.S. Thayer, and A.G. Yodh, "Regional imager for low resolution functional imaging of the brain with diffusing near-infrared light," Photochemistry and Photobiology **67**, 33-40 (1998).
8. T. McBride, B. W. Pogue, E. Gerety, S. Poplack, Ulf Osterberg, B. Pogue and K. Paulsen, "Spectroscopic diffuse optical tomography for the quantitative assessment of hemoglobin concentration and oxygen saturation in breast tissue," Appl. Opt. **38**, 5480-5490 (1999).
9. M. A. Franceschini, K. T. Moesta, S. Fantini, G. Gaida, E. Gratton, H. Jess, M. Seeber, P. M. Schlag, M. Kashke, "Frequency-domain techniques enhance optical mammography: initial clinical results," Proc. Of Nat. Ac. of Sci. **94**, 6468-6473 (1997).
10. J. B. Fishkin, O. Coquoz, E.R. Anderson, M. Brenner, and B. J. Tromberg, "Frequency-domain photon mogration measurements of normal and malignant tissue optical properties in human subject," Appl. Opt. **36**,10-20 (1997).
11. T. L. Troy, D. L. Page, and E. M. Sevick-Muraca, "Optical properties of normal and diseased breast tissues: prognosis for optical mammography," Journal of Biomedical Optics **1**, 342-355 (1996).
12. R. J. Grable, D. P. Rohler and S. KLA , "Optical tomography breast imaging," in Proceedings of Optical Tomography and Spectroscopy of Tissue: Theory, Instrumentation, Model, and Human Studies II , B. Chance and R. Alfano , eds, Proc. SPIE 2979, 197-210 (1997).
13. Y. Yao, Y. Wang, Y. Pei, W. Zhu, and RL. Barbour, "Frequency-domain optical imaging of absorption and scattering distributions by a Born iterative method," J. Opt. Soc. Am. A **14**, 325-341 (1997).

14. H. Jiang, K. Paulsen, Ulf Osterberg, B. Pogue and M. Patterson, ”Optical image reconstruction using frequency-domain data: simulations and experiments,” J. Opt. Soc. Am. A. **2**, 253-266 (1995).

15. X. Li, T. Durduran and A. Yodh, B. Chance and D.N. Pattanayak, “Diffraction tomography for biomedical imaging with diffuse-photon density waves, ” Opt. Lett. **22,** 573-575 (1998).

16. C. Matson and H. Liu, ‘‘Backpropagation in turbid media,” J. Opt. Soc. Am. A. **16(6),** 1254-1265 (1999).

16. M. A. O’Leary, “Imaging with diffuse photon density waves,” Ph.D. dissertation (University of Pennsylvania, Philadelphia, Pa., 1996).

17. K. Paulsen, P. Meaney, M. Moskowitz, and J. Sullivan, Jr., ‘‘A dual mesh scheme for finite element based reconstruction algorithms,” IEEE Trans. On Medical Imaging **14(3)**, 504-514 (1995).

18. S. Arridge and M. Schweiger, ”Photon-measurement density functions, Part I: analytical forms,” Appl. Opt. **34**, 7395-7409 (1995).

19. S. Arridge and M. Schweiger, “Photon-measurement density functions, Part II: Finite-element-method calculations,” Appl. Opt. **34**, 8026-8037 (1995).

20. Q. Zhu, T. Dunrana, M. Holboke, V. Ntziachristos and A. Yodh , “Imager that combines near infrared diffusive light and ultrasound,” Opt. Lett., **24(15),** 1050-1052 (1999).

21. Q. Zhu, D. Sullivan , B. Chance , and T. Dambro , “Combined ultrasound and near infrared diffusive light imaging,” IEEE Trans, Ultrason. Ferroelect. Freq. Contr. **46(3),** 665-678 (1999).

22. Q. Zhu, E. Conant and B. Chance, ''Optical imaging as an adjunct to sonograph in differentiating benign from malignant breast lesions,'' Journal of Biomedical Optics **5(2)**, 229-236 (2000).

23. Q. Zhu, NG. Chen, DQ, Piao, PY. Guo and XH. Ding," Design of near infrared imaging probe with the assistance of ultrasound localization," Appl. Opt. July No.40 (2001).

24. M. Jholboke, B. J. Tromberg, X. Li, N. Shah, J. Fishkin, D. Kidney, J. Butler, B. Chance, and A. G. Yodh, "Three-dimentional diffuse optical mammography with ultrasound localization in human subject," Journal of Biomedical Optics **5(2)**, 237-247 (2000).

25. W. Zhu, Y. Wang and J. Zhang, "Total least-squares reconstruction with wavelets for optical tomography," J. Opt. Soc. Am. A. **15,** 2639-2650 (1998).

26. PC. Li, W. Flax, E. S. Ebbini and M. O'Donnell, ''Blocked element compensation in phased array imaging," IEEE Trans, Ultrason. Ferroelect. Freq. Contr. **40(4)**, 283-292 (1993).

27. G. H. Golub, ''Some modified matrix eigenvalue problems," SIAM (Soc. Ind. Appl. Math.) Rev. **15**, 318-334 (1973).

Table 1. Parameters of reconstructed images for deep high ($\mu_a = 0.25\,\text{cm}^{-1}$) and low ($\mu_a = 0.1\,\text{cm}^{-1}$) contrast targets. The fitted background μ_a and μ_s' are 0.015 cm^{-1} and 5.36 cm^{-1}, respectively. $\hat{\mu}_{a(\max)}$ is the measured maximum value of the reconstructed absorption coefficient map, FWHM is defined as the geometric mean of the widths measured at longer and shorter axes of the elliptical image lobe.

Probe type	No-hole	2 ×2	3×3
High contrast			
$\hat{\mu}_{a(\max)}$ (cm^{-1})	0.251	0.234	0.104
FWHM (cm)	1.85	1.91	2.44
Artifacts (dB)	Background (-22dB)	background	-14.3
Low contrast			
$\hat{\mu}_{a(\max)}$ (cm^{-1})	0.105	0.111	0.064
FWHM (cm)	2.02	1.83	2.16
Artifacts (dB)	-6.90	-8.10	-5.65

Table 2. Parameters of reconstructed images for shallow high ($\mu_a = 0.25\,\text{cm}^{-1}$) and low ($\mu_a = 0.1\,\text{cm}^{-1}$) contrast targets. The fitted background μ_a and μ_s' are 0.015cm^{-1} and $5.35\ \text{cm}^{-1}$, respectively.

Probe type	No-hole	2 ×2	3×3
High contrast			
$\hat{\mu}_{a(\max)}$ (cm^{-1})	0.250	0.194	0.118
FWHM (cm)	1.32	1.61	2.08
Artifacts (dB)	-7.98	-12.7	-9.76
Low contrast			
$\hat{\mu}_{a(\max)}$ (cm^{-1})	0.100	0.091	0.042
FWHM (cm)	1.88	2.11	3.17
Artifacts (dB)	-6.25	-7.44	-0.65

Figure Captions

Figure1. Schematic arrangement of NIR source and detector fibers on the probe. Small solid circles are source fibers and bigger solid cycles are detector fibers.

Figure 2. Picture of an experimental probe. An ultrasound array of $8\times 8 = 64$ transducers occupies the central 3×3 cm^2 area, and 12 dual wavelength source fibers and 8 detector fibers are deployed at the periphery.

Figure 3. Schematic of the NIR frequency domain imaging system. The modulation frequency is 140MHz. The 12 dual-wavelength source channels are switched on sequentially by a PC and 8 detector channels receive signals in parallel.

Figure 4. (a) Log($\rho^2_{\alpha\beta} A_{\alpha\beta}$) vs. distancev $\rho_{\alpha\beta}$ after calibration. (b) phase $\phi_{\alpha\beta}$ vs. distance $\rho_{\alpha\beta}$ after calibration.

Figure 5. Schematic of our ultrasound scanner. 64 ultrasound transducers are connected to 64 parallel transmission and reception channels. The transmission part consists of 64 high voltage pulsers, which can be controlled by computer generated delay profiles. The reception part consists of 64 two-stage amplifiers and A/D converters.

Figure 6. Ultrasound subarray scanning configuration.

Figure 7. Picture of our combined system. NIR system (top) and ultrasound system (bottom) are mounted on a hospital cart.

Figure 8. Reconstructed NIR images of deeper targets (2.5 cm in depth, 1 cm in diameter, and fitted background μ_a and $\mu_s^{'}$ are 0.015 cm^{-1} and 5.36 cm^{-1}, respectively). The left column corresponds to images of a high contrast target ($\mu_a = 0.25\,cm^{-1}$) obtained from different probe configurations, while the right column corresponds to images of a low contrast target ($\mu_a = 0.1\,cm^{-1}$). Each row is related to a specific hole size: 1) No hole (a and b); 2) $2\times 2cm^{2}$ (c and d); and 3) 3×3 cm^2 (e and f).

Figure 9. Reconstructed NIR images for shallow targets (1.5 cm in depth, 1 cm in diameter, and fitted background μ_a and $\mu_s^{'}$ are 0.015 cm^{-1} and 5.36 cm^{-1}, respectively). The left column corresponds to images of a high contrast target ($\mu_a = 0.25\,cm^{-1}$), while the right column corresponds to images of a low contrast target ($\mu_a = 0.1\,cm^{-1}$). Each row is related to a specific hole size: 1) No hole (a and b); 2) 2×2 cm^2 (c and d); and 3) 3×3 cm^2 (e and f).

Figure 10. A deep target (2.5 cm in depth, 1 cm in diameter) of low optical contrast ($\mu_a = 0.10\,cm^{-1}$, and fitted background μ_a and $\mu_s^{'}$ are 0.02 cm^{-1} and 5.08 cm^{-1}, respectively). (a) A-scan line of the reflected ultrasound pulse-echo signal indicating the target depth. (b) absorption image of the low contrast target obtained from optical only reconstruction. (c) ultrasound guided reconstruction at target depth.

Figure 11. Simultaneously obtained ultrasound and NIR absorption images. The fitted background μ_a and $\mu_s^{'}$ are 0.017 cm^{-1} and 4.90 cm^{-1}, respectively. (a) ultrasound and (b) NIR

absorption image of two high contrast targets (target $\mu_a = 0.25\,\text{cm}^{-1}$). (c) ultrasound and (d) NIR image of two low contrast targets (target $\mu_a = 0.10\,\text{cm}^{-1}$). In both high and low contrast cases, the two targets were located at 2.5 cm depth.

Figure 12. (a) and (c) are –6 dB contour plots of ultrasound images shown in Fig. 11 (a) and (c). The outer contour is –6 dB from the peak and the contour spacing is 1 dB. (b) and (d) are corresponding NIR absorption maps reconstructed in target regions specified by ultrasound.

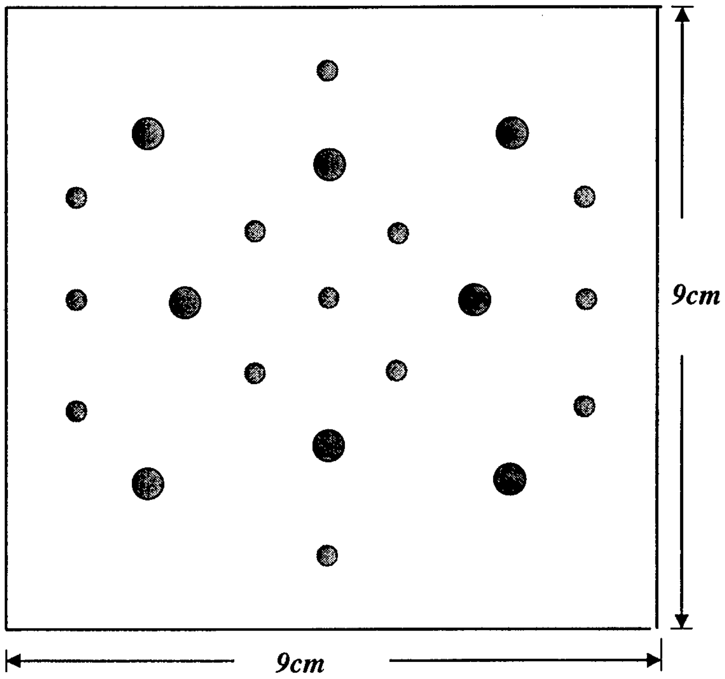

Fig.1.

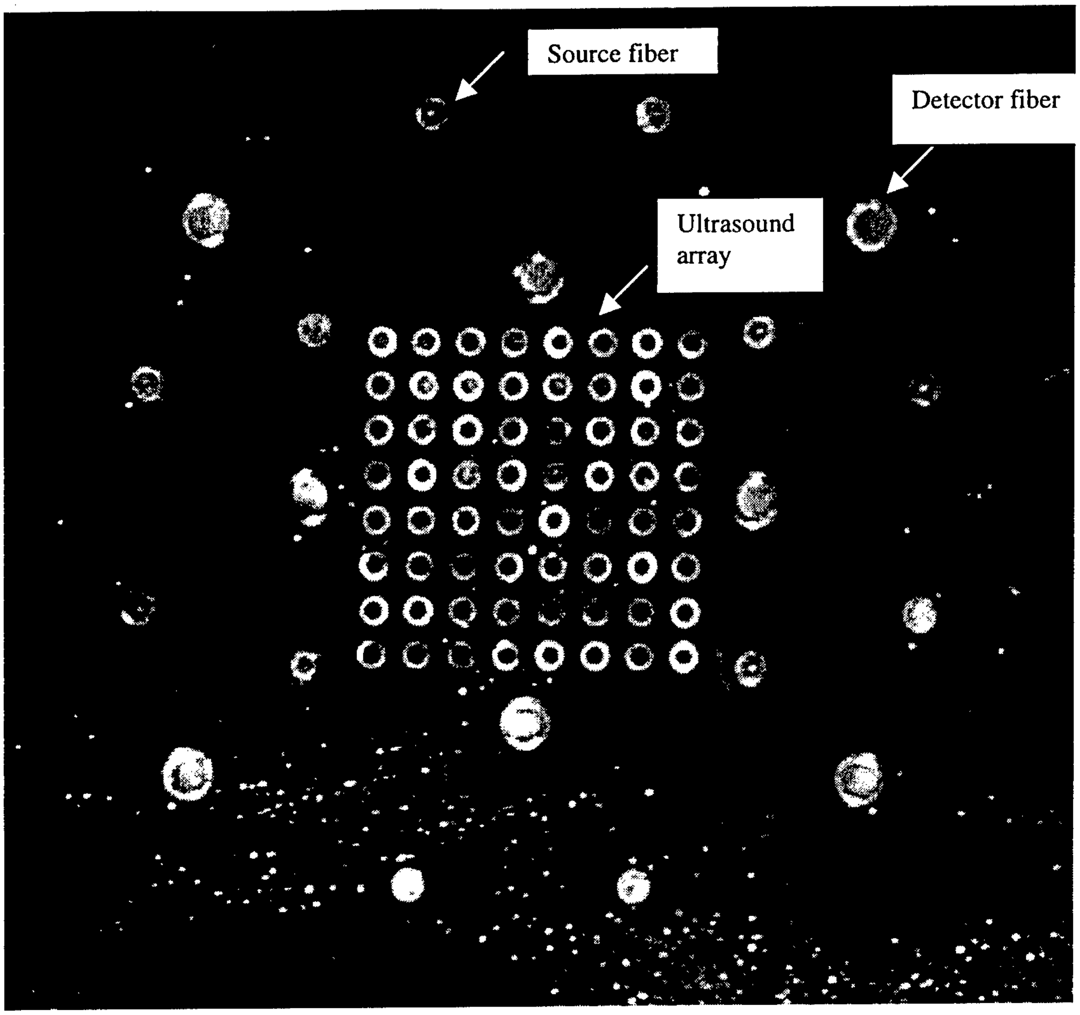
Source fiber
Detector fiber
Ultrasound array

Fig.2

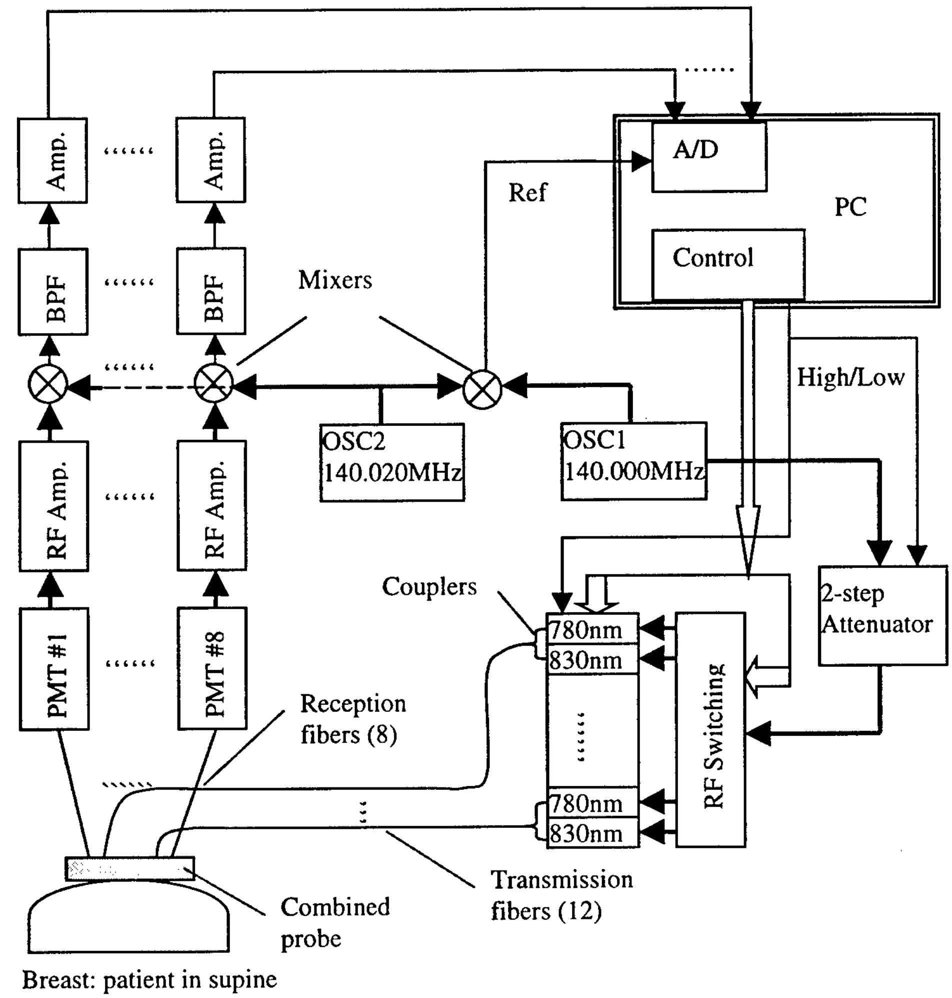

Amp.
Amp.
A/D
Ref
PC
Control
BPF
BPF
Mixers
High/Low
OSC2
140.020MHz
OSC1
140.000MHz
RF Amp.
RF Amp.
Couplers
780nm
830nm
780nm
830nm
2-step
Attenuator
RF Switching
PMT #1
PMT #8
Reception
fibers (8)
Transmission
fibers (12)
Combined
probe
Breast: patient in supine

Fig.3.

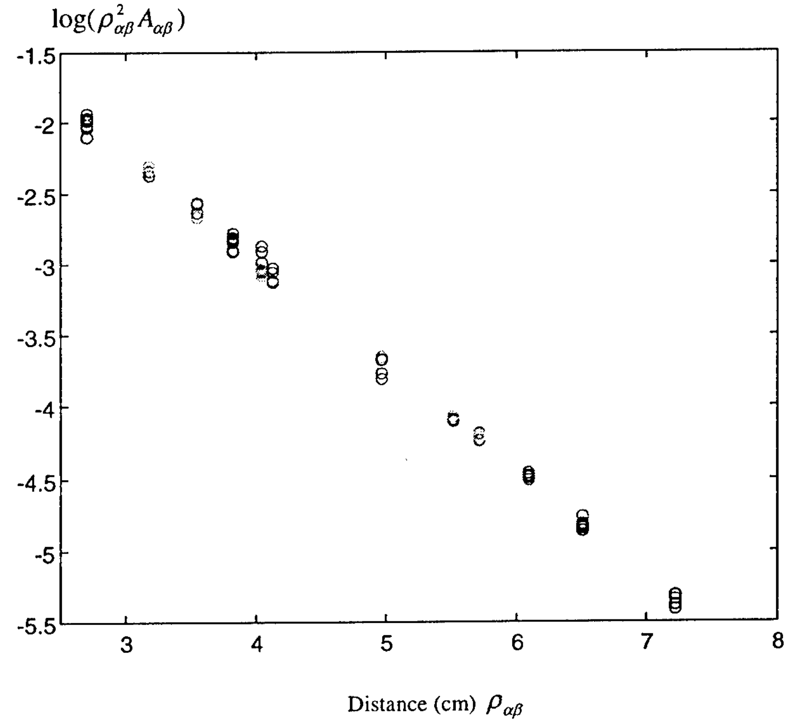

$\log(\rho_{\alpha\beta}^2 A_{\alpha\beta})$
-1.5
-2
-2.5
-3
-3.5
-4
-4.5
-5
-5.5
3
4
5
6
7
8
Distance (cm) $\rho_{\alpha\beta}$

(a)

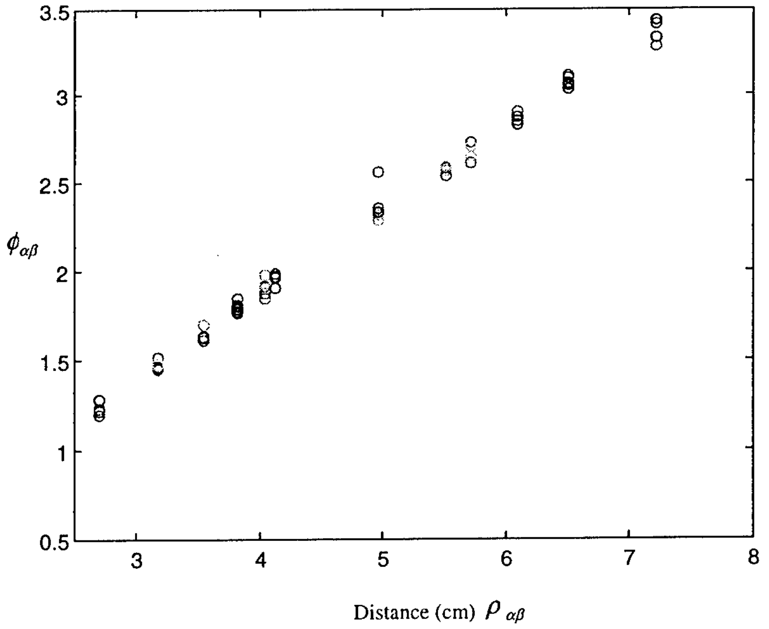

3.5
3
2.5
2
1.5
1
0.5
$\phi_{\alpha\beta}$
3
4
5
6
7
8
Distance (cm) $\rho_{\alpha\beta}$

(b)

Fig. 4.

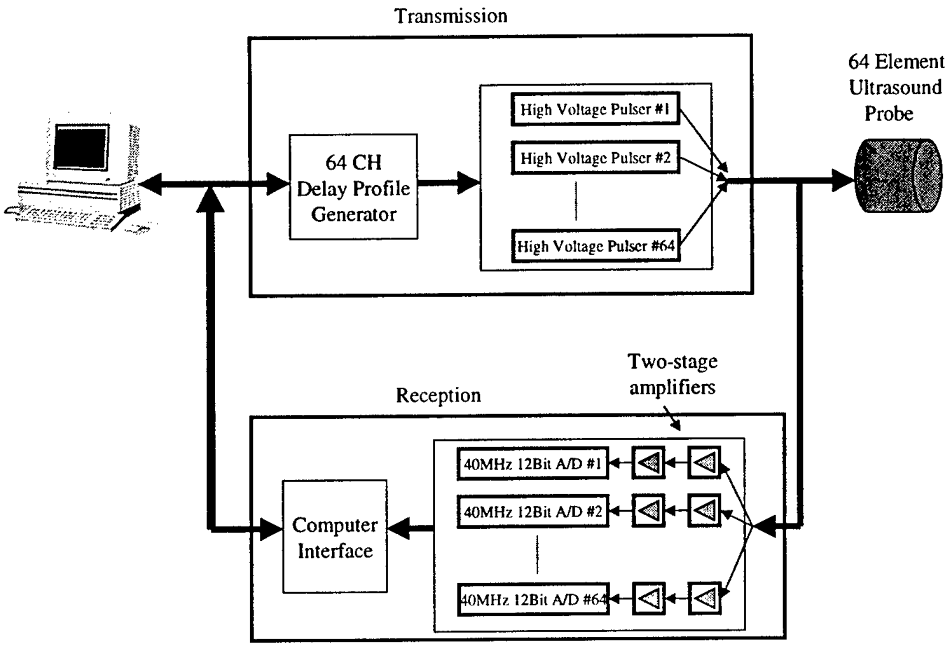
Transmission
64 Element
Ultrasound
Probe
64 CH
Delay Profile
Generator
High Voltage Pulser #1
High Voltage Pulser #2
High Voltage Pulser #64
Two-stage
amplifiers
Reception
40MHz 12Bit A/D #1
40MHz 12Bit A/D #2
40MHz 12Bit A/D #64
Computer
Interface

Fig.5.

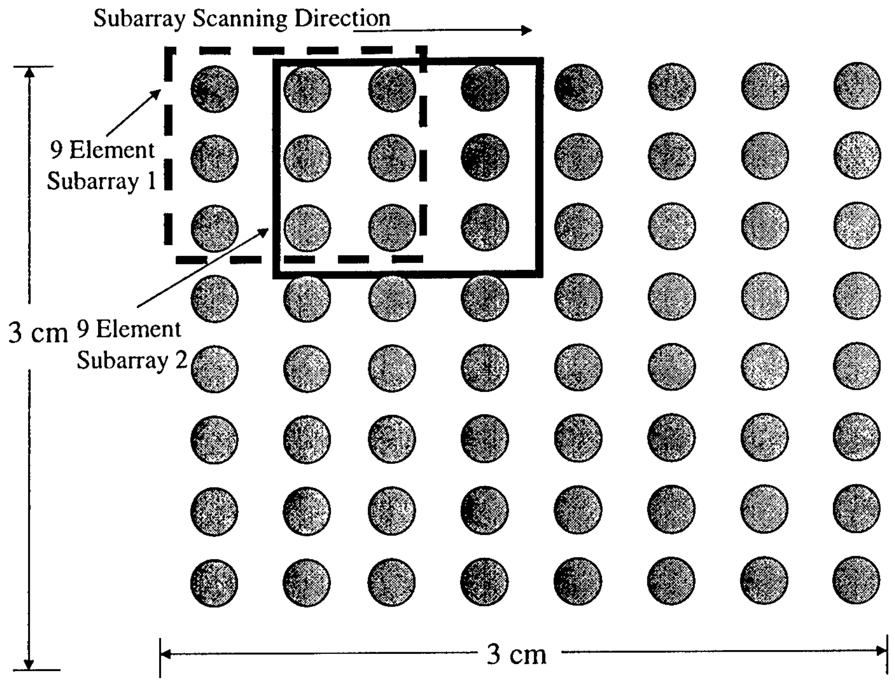
Subarray Scanning Direction
9 Element Subarray 1
9 Element Subarray 2
3 cm
3 cm

Fig. 6

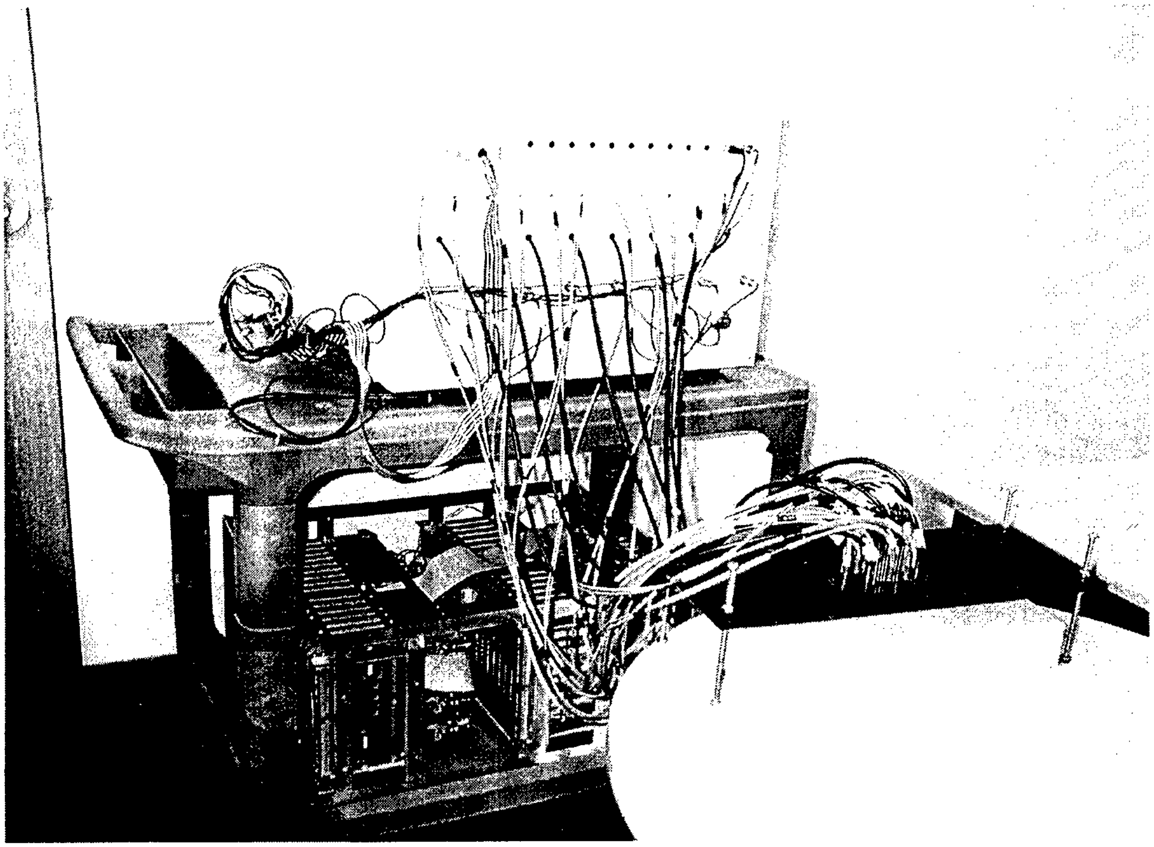

Fig.7

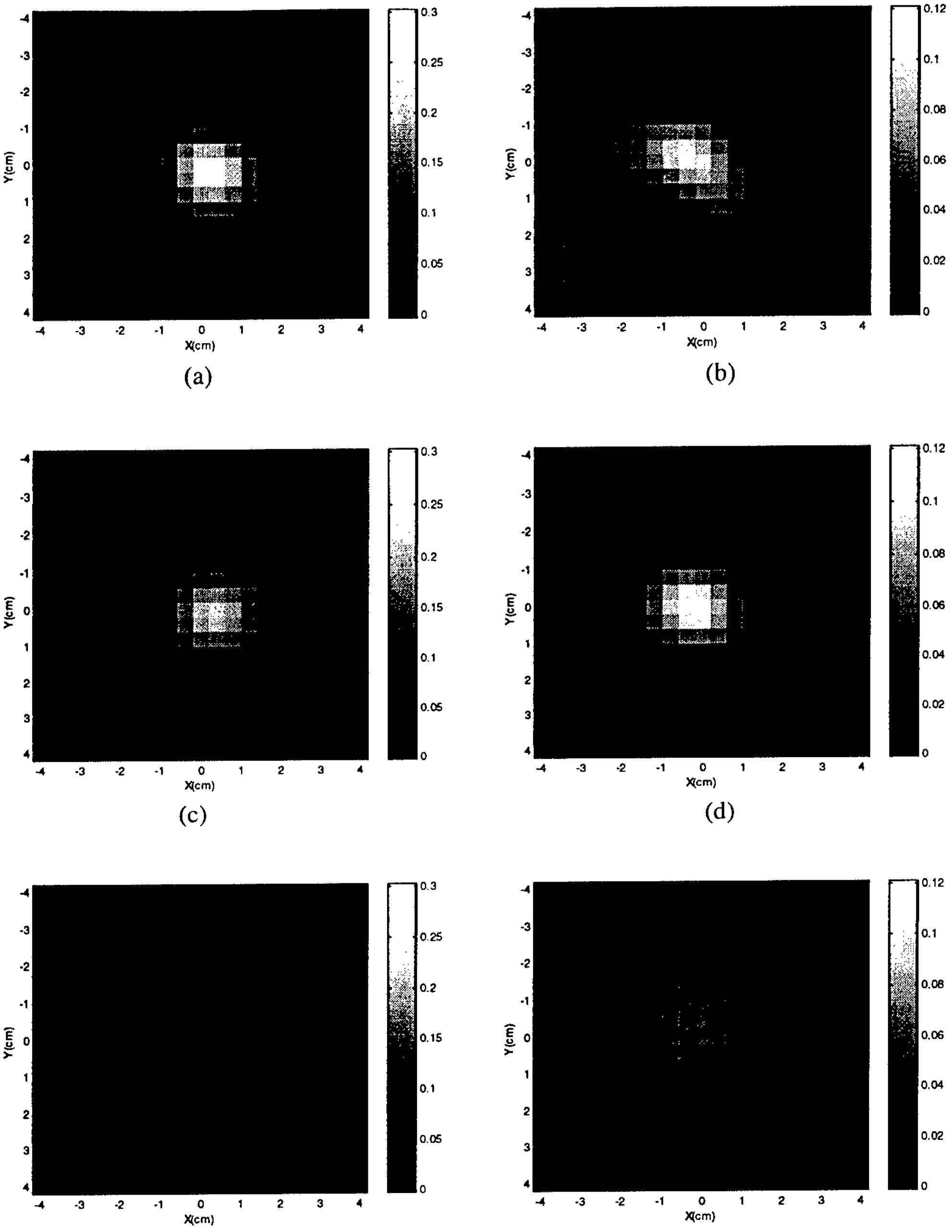
Y(cm)
X(cm)
-4
-3
-2
-1
0
1
2
3
4
0.3
0.25
0.2
0.15
0.1
0.05
0
0.12
0.1
0.08
0.06
0.04
0.02
0

(a) (b) (c) (d) (e) (f)

Fig.8

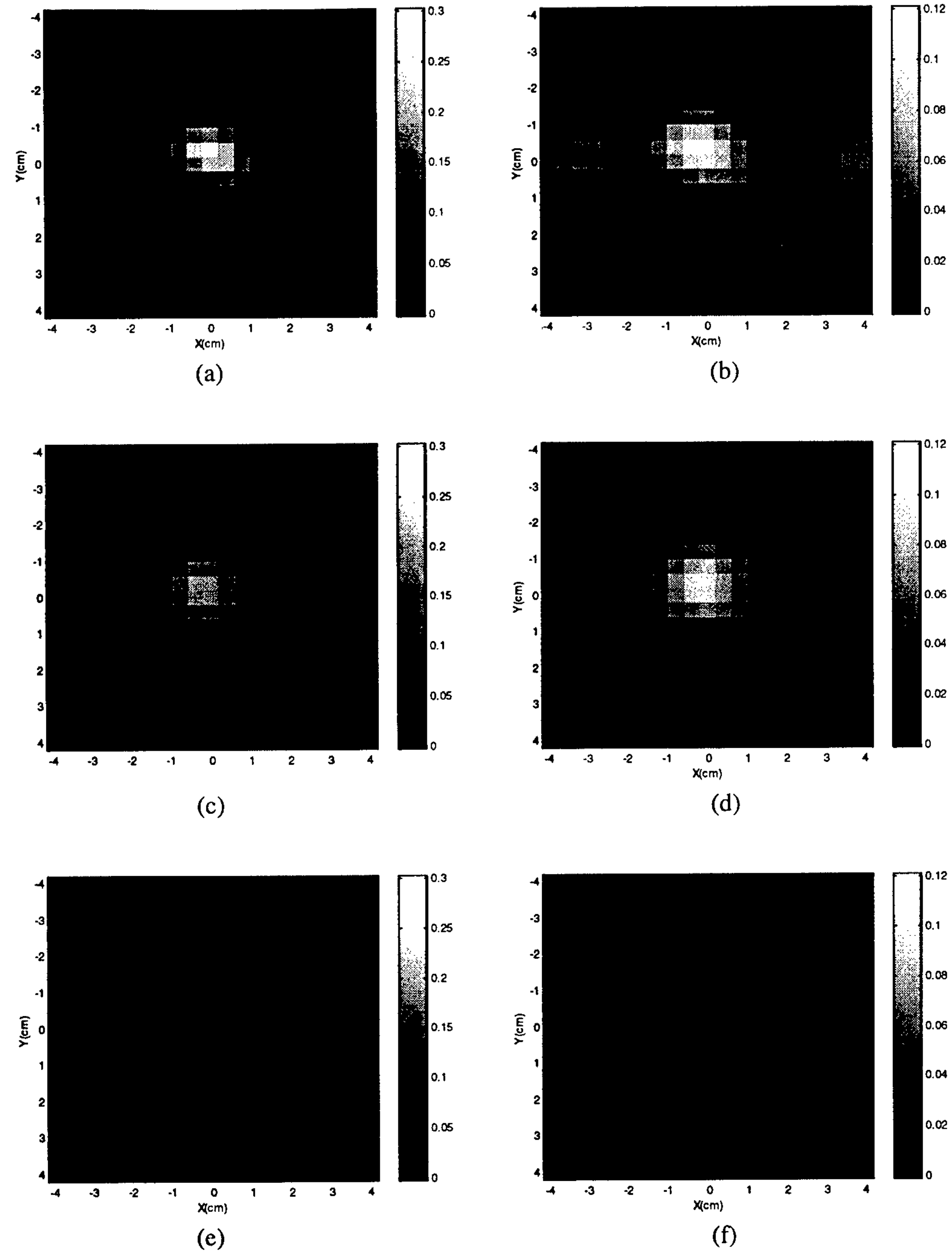
Y(cm)
X(cm)
-4
-3
-2
-1
0
1
2
3
4
0.3
0.25
0.2
0.15
0.1
0.05
0
0.12
0.1
0.08
0.06
0.04
0.02
0
(a)
(b)
(c)
(d)
(e)
(f)

Fig.9

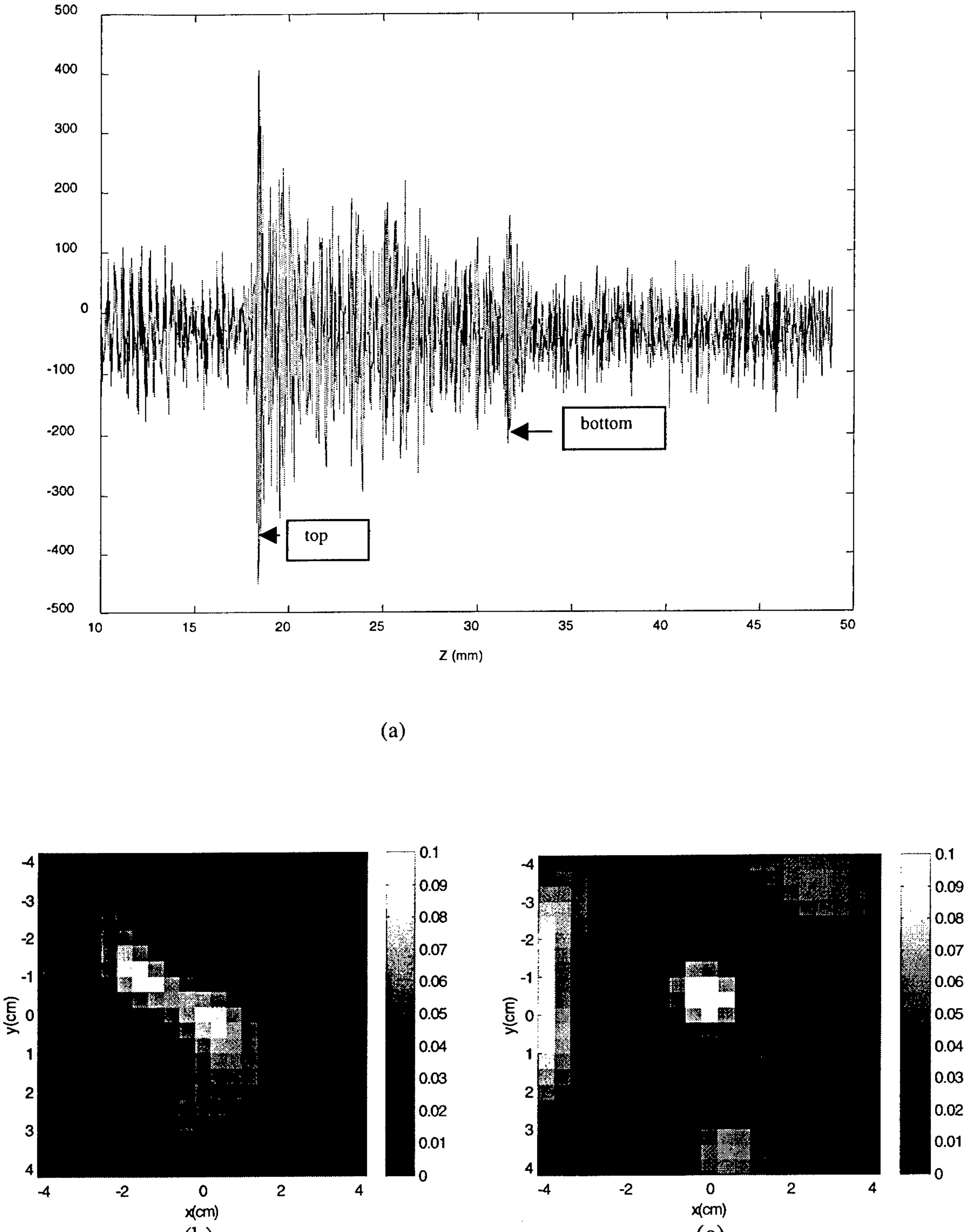
500
400
300
200
100
0
-100
-200
-300
-400
-500
10
15
20
25
30
35
40
45
50
Z (mm)
top
bottom
-4
-3
-2
-1
0
1
2
3
4
y(cm)
x(cm)
0.1
0.09
0.08
0.07
0.06
0.05
0.04
0.03
0.02
0.01
0

(a)

(b)

(c)

Fig.10

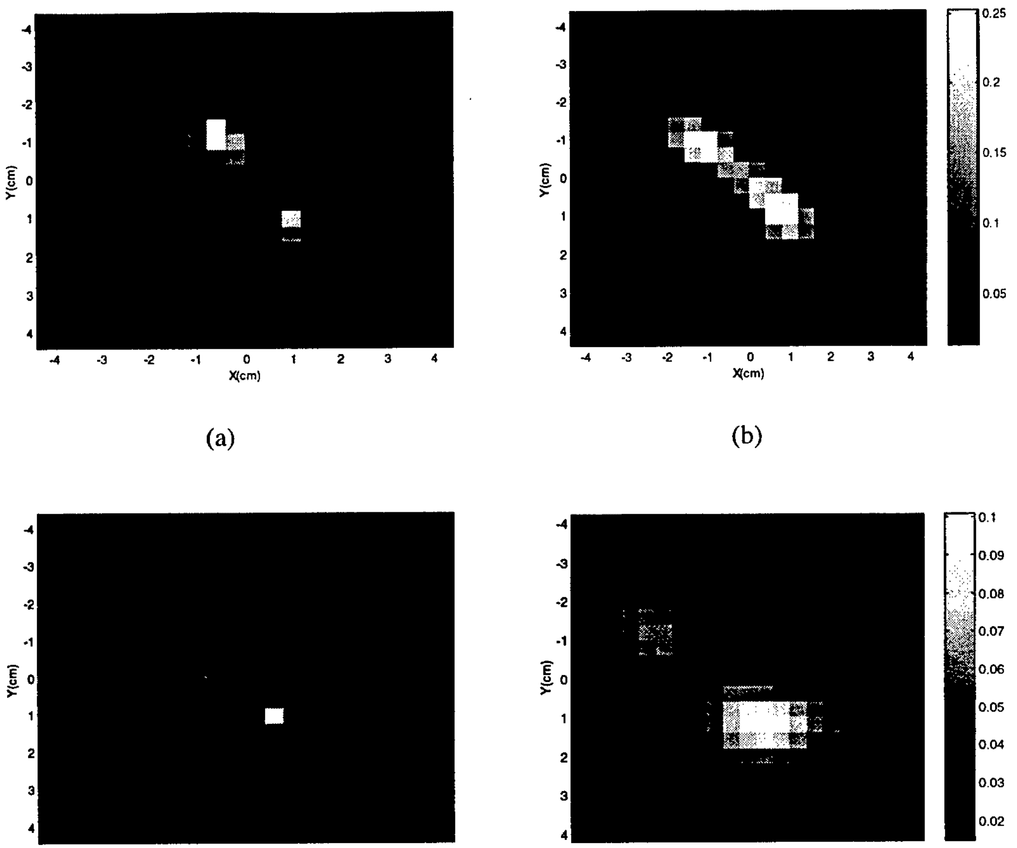
Y(cm)
X(cm)
-4
-3
-2
-1
0
1
2
3
4
0.25
0.2
0.15
0.1
0.05
0.1
0.09
0.08
0.07
0.06
0.05
0.04
0.03
0.02

(a) (b)

(c) (d)

Fig.11.

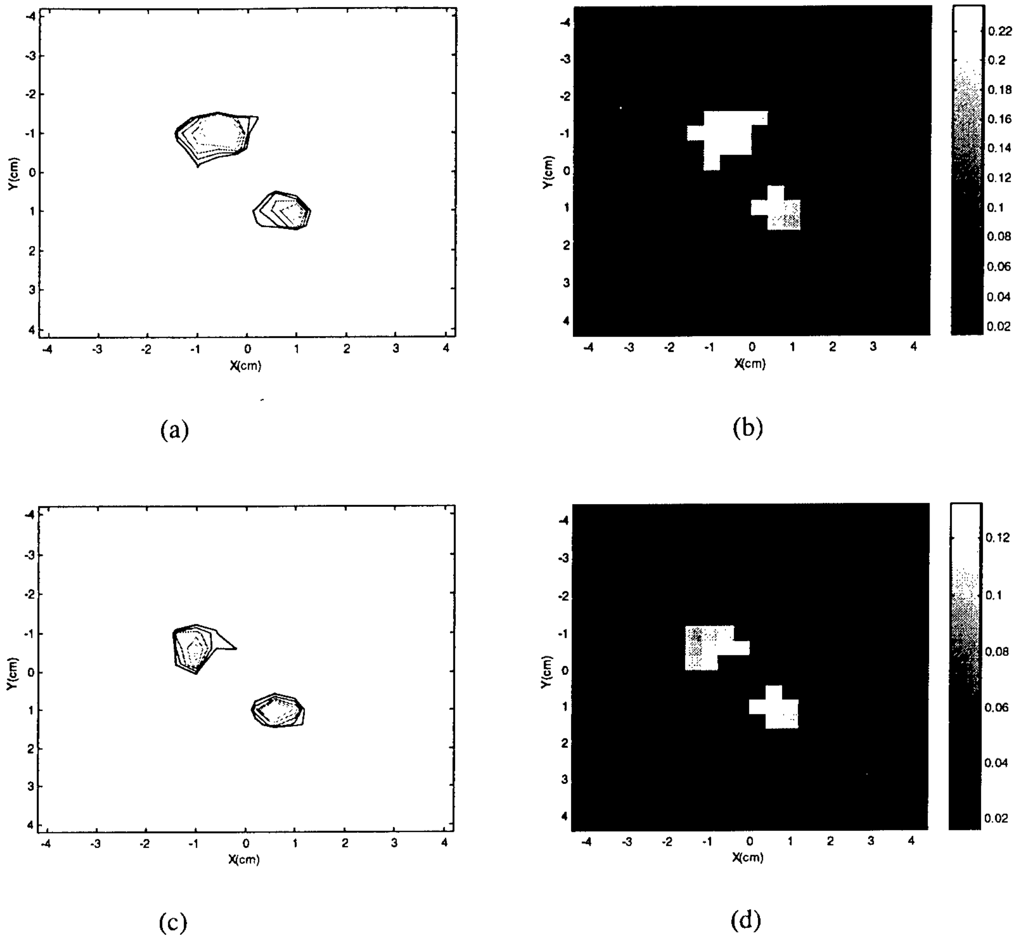

Y(cm)
X(cm)
-4
-3
-2
-1
0
1
2
3
4
0.22
0.2
0.18
0.16
0.14
0.12
0.1
0.08
0.06
0.04
0.02
0.12
0.1
0.08
0.06
0.04
0.02

(a) (b)

(c) (d)

Fig. 12